Article

Cell Reports

Phosphatidylserine Externalization Results from and Causes Neurite Degeneration in *Drosophila*

Graphical Abstract

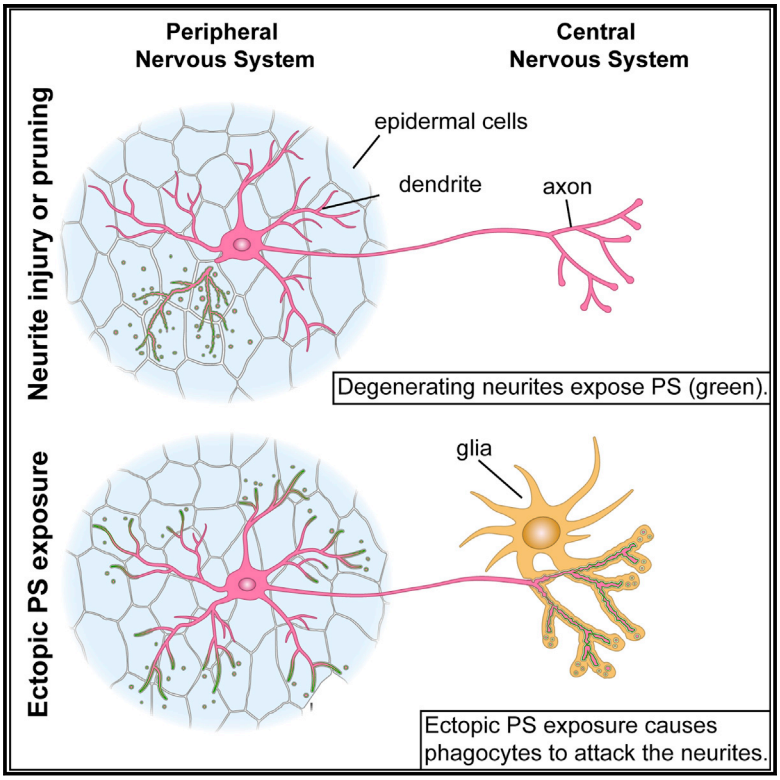

Authors

Maria L. Sapar, Hui Ji, Bei Wang, ..., Xingjie Ren, Jian-Quan Ni, Chun Han

Correspondence

chun.han@cornell.edu

In Brief

Using *in vivo* phosphatidylserine (PS) sensors, Sapar et al. reveal dynamic patterns of PS exposure on degenerating dendrites in *Drosophila*. Flippase knockout and scramblase overexpression lead to ectopic PS exposure on distal dendrites and context-dependent neurite degeneration. Lactadherin potentiates phagocytes to destruct PS-exposing dendrites, independent of its integrin-interaction domain.

Highlights

- PS is exposed on degenerating dendrites in a specific spatiotemporal pattern
- PS exposure on injured dendrites depends on NAD^+ depletion, not caspase activity
- Ectopic PS exposure on live neurons causes phagocytes to engulf distal neurites
- Lactadherin C1C2 domain potentiates phagocytes to destruct PS-exposing dendrites

Sapar et al., 2018, Cell Reports *24*, 2273–2286
August 28, 2018
https://doi.org/10.1016/j.celrep.2018.07.095

CellPress

Cell Reports
Article

Phosphatidylserine Externalization Results from and Causes Neurite Degeneration in *Drosophila*

Maria L. Sapar,[1,4] Hui Ji,[1,4] Bei Wang,[1] Amy R. Poe,[1] Kush Dubey,[1] Xingjie Ren,[2,3] Jian-Quan Ni,[2] and Chun Han[1,5,*]
[1]Weill Institute for Cell and Molecular Biology, Department of Molecular Biology and Genetics, Cornell University, Ithaca, NY 14853, USA
[2]Gene Regulatory Lab, School of Medicine, Tsinghua University, Beijing 100084, China
[3]Present address: Institute for Human Genetics, Department of Neurology, University of California, San Francisco, San Francisco, CA 94143, USA
[4]These authors contributed equally
[5]Lead Contact
*Correspondence: chun.han@cornell.edu
https://doi.org/10.1016/j.celrep.2018.07.095

SUMMARY

Phagocytic clearance of degenerating dendrites or axons is critical for maintaining tissue homeostasis and preventing neuroinflammation. Externalized phosphatidylserine (PS) has been postulated to be an "eat-me" signal allowing recognition of degenerating neurites by phagocytes. Here we show that in *Drosophila*, PS is dynamically exposed on degenerating dendrites during developmental pruning and after physical injury, but PS exposure is suppressed when dendrite degeneration is genetically blocked. Ectopic PS exposure via phospholipid flippase knockout and scramblase overexpression induced PS exposure preferentially at distal dendrites and caused distinct modes of neurite loss that differ in larval sensory dendrites and in adult olfactory axons. Surprisingly, extracellular lactadherin that lacks the integrin-interaction domain induced phagocyte-dependent degeneration of PS-exposing dendrites, revealing an unidentified bridging function that potentiates phagocytes. Our findings establish a direct causal relationship between PS exposure and neurite degeneration *in vivo*.

INTRODUCTION

The nervous system requires active monitoring and maintenance. During development, erroneous neuronal processes and excessive connections between neurons are trimmed (Chung et al., 2015; Luo and O'Leary, 2005). Animals undergoing metamorphosis prune existing neural circuits before establishing new ones (Emoto, 2011; Schuldiner and Yaron, 2015). Furthermore, physical insults can cause neuronal processes to degenerate. Consequently, efficient clearance of pruned or damaged neurites by phagocytes is critical for maintaining tissue homeostasis and preventing inflammation. Failure of clearance may cause secondary neurodegeneration and autoimmune disease (Nagata, 2010; Salter and Stevens, 2017).

How phagocytes recognize and clear neurites destined to be removed, while sparing other parts of the same neuron, is unclear *in vivo*. In comparison, apoptotic cell recognition by phagocytes is known to rely on "eat-me" signals exposed on the surface of dying cells (Ravichandran, 2010). A well-defined eat-me signal is phosphatidylserine (PS), a phospholipid found exclusively in the cytoplasmic leaflet of most healthy cells (Segawa and Nagata, 2015). During apoptosis, PS is externalized and flags the cell for engulfment by directly or indirectly interacting with engulfment receptors on phagocytes. The asymmetric PS distribution across the plasma membrane is established and maintained by aminophospholipid flippases encoded by the P4-ATPase family (Natarajan et al., 2004; Tang et al., 1996), whereas PS externalization is promoted by phospholipid scramblases. TMEM16F is a calcium-dependent scramblase required for PS exposure in platelet activation (Fujii et al., 2015; Suzuki et al., 2010). XKR family members, including mammalian XKR8, are caspase-activated scramblases that stimulate PS exposure in apoptotic cells (Suzuki et al., 2013).

Recent evidence links PS exposure to neurite degeneration. Dorsal root ganglion neurons induced to degenerate *in vitro* expose PS on their axons (Kim et al., 2010; Wakatsuki et al., 2017). Knockdown of the scramblase XKR8 or a lipid translocase ABC1 reduces PS exposure during degeneration (Wakatsuki and Araki, 2017). Moreover, PS recognition pathways are implicated in the phagocytosis of neurons. The mammalian TAM receptors (Tyro3, Axl, and Mertk) mediate phagocytosis of apoptotic cells by interacting with two PS binding proteins, Growth arrest-specific protein 6 (Gas6) and Protein S (Pros1) (Lemke, 2013; Lew et al., 2014). Loss of *Axl* and *Mertk* in the adult mouse CNS results in impaired cell clearance after viral infection (Tufail et al., 2017) and accumulation of apoptotic cells in the CNS (Fourgeaud et al., 2016). Another secreted PS-binding protein lactadherin (alternatively called MFG-E8), which interacts with the engulfment receptor $\alpha_v\beta_3$ integrin (Andersen et al., 2000; Hanayama et al., 2002), stimulates the phagocytosis of PS-exposing photoreceptor outer segments (POSs) in the mouse retina (Nandrot et al., 2007) and that of viable neurons during neuroinflammation induced by lipopolysaccharide treatment (Fricker et al., 2012). In addition, exogenous PS treatment has been shown to be neuroprotective in a degenerative disease model (Naftelberg et al., 2016).

Despite these evidences, several important questions regarding the roles of PS exposure in neurodegeneration remain unanswered. PS exposure induced on live neurons can lead to phagocytosis by co-cultured microglia (Brown and Neher, 2014). However, PS exposure on live cells does not necessarily lead to engulfment *in vivo* (Appelt et al., 2005; Heemskerk et al., 2002; Segawa et al., 2011). Therefore, direct *in vivo* evidence is required to demonstrate the sufficiency of PS exposure in driving neuronal degeneration. Mutations in mouse *Atp8a2*, a P4-ATPase gene, are associated with axon degeneration (Zhu et al., 2012), but the mechanism is unknown. Because PS exposure is associated with cell-autonomous membrane vesicle shedding in many contexts (Lima et al., 2009; Morel et al., 2004; Muralidharan-Chari et al., 2009), it is unclear whether PS exposure can by itself induce cell-autonomous loss of neurite membranes or whether degeneration is a consequence of phagocyte activity. Additionally, both flippase inactivation and scramblase activation can result in PS exposure in non-apoptotic cells (Segawa and Nagata, 2015), but whether they produce similar effects in neurons remains to be determined. Lastly, it is unknown whether different spatial domains of the same neuron are equally sensitive to disruptions of PS asymmetry under pathological conditions.

To address these questions, we utilized the *Drosophila* dendritic arborization (da) neurons that extend dendritic arbors underneath the larval epidermis (Grueber et al., 2002; Han et al., 2012; Kim et al., 2012). During dendrite remodeling and after dendrite injury, epidermal cells function as the primary phagocytes that break down and engulf da dendrites (Han et al., 2014) in a process similar to the clearance of injured sensory axons by zebrafish epidermal cells (Rasmussen et al., 2015). In this study, we examined the spatiotemporal pattern of PS exposure on degenerating dendrites using genetically coded GFP-tagged PS binding proteins (Mapes et al., 2012) and investigated the roles of nicotinamide adenine dinucleotide (NAD^+) depletion and caspase activity in injury-induced PS exposure. Furthermore, we studied the effects of ectopically induced PS exposure in uninjured neurons in the larval peripheral nervous system (PNS) and the adult CNS. Lastly, we found that extracellular lactadherin potentiates *Drosophila* epidermal cells to destruct PS-exposing dendrites through an unidentified bridging domain. Together, our study reveals *in vivo* dynamics of PS exposure on degenerating neurites and establishes a direct functional association between PS exposure and phagocytosis-dependent neurite loss in *Drosophila*.

RESULTS

PS Is Dynamically Exposed on Degenerating Dendrites after Injury and during Dendrite Remodeling

Building on two PS-binding proteins, Annexin V (AV) (Koopman et al., 1994) and the lactadherin C1C2 domain (LactC1C2) (Andersen et al., 2000), we developed an *in vivo* system in *Drosophila* larvae to visualize surface PS externalization on cells exposed to the hemolymph. The GFP-tagged, secreted forms of these proteins (Mapes et al., 2012) are referred to as AV-GFP and GFP-Lact. LactC1C2 specifically binds to PS but lacks the integrin-interacting motif of the full-length protein (Hanayama et al., 2002). AV-GFP and GFP-Lact secreted by the fat body diffuse to da neuron dendrites labeled by CD4-tdTom (Han et al., 2011) via the hemolymph and decorate the outer surface of the branches exposing PS (Figure 1A).

We examined PS exposure of class IV da (C4 da) neurons both after dendrite injury and during dendrite pruning. At 4–5 hr after laser injury, severed dendrites actively underwent blebbing and fragmentation (Han et al., 2014; Tao and Rolls, 2011) and exhibited robust labeling by both AV-GFP (Figures 1B–1B″, blue arrows, n = 29 neurons) and GFP-Lact (Figures 1C–1C″, blue arrows, n = 22 neurons). In contrast, uninjured dendrites of ablated neurons (Figures 1B–1C″, yellow arrowheads) or healthy neurons (Figure S1A–S1A″) did not show any labeling. PS sensor labeling correlated with the stage of dendrite degeneration: smooth and healthy-looking branches often did not show obvious labeling, whereas branches with roughened surfaces or blebs usually showed strong labeling. As controls, AV(mut)-GFP (Figures S1B–S1B″; n = 24 neurons) and GFP-Lact(mut) (Figures S1C–S1C″; n = 17 neurons), which carry mutations that abolish their ability to interact with PS (Dubois et al., 1998; Lin et al., 2007; Mapes et al., 2012), did not label any injured dendrites.

For dendrite pruning, we used time-lapse imaging to examine PS exposure on C4 da dendrites, which exhibit asynchronized severing and fragmentation (Kanamori et al., 2013). AV-GFP consistently labeled the branches that were degenerating, but not before branches showed any sign of degeneration (Figures 1D–1D″; Video S1). GFP-Lact labeled pruned dendrites (Figures 1E–1E″; Video S2) less consistently than AV-GFP. During metamorphosis, many larval tissues underwent large-scale apoptosis, possibly sequestering GFP-Lact away from pruned dendrites. Nevertheless, these results demonstrate that PS is specifically exposed on degenerating dendrites both after injury and during pruning.

To further investigate the timing of PS exposure on degenerating dendrites, we recorded AV-GFP labeling of injured dendrites in larvae using long-term time-lapse imaging (Poe et al., 2017), which began at 1.5–2 hr after injury (AI) and lasted 5–7 hr, long enough to capture most of the dendrite degeneration process (Han et al., 2014). Uninjured dendrites exhibit normal growth dynamics (e.g., extension, retraction, and turning) and no AV-GFP binding, signifying the health of the larvae (Video S3). In contrast, severed dendritic arbors exhibit specific spatiotemporal patterns of AV-GFP labeling (Video S3). The peak of AV-GFP binding usually started at terminal branches and then spread to low-order branches, as apparent in color-coded timing of AV-GFP peak signal on the dendritic arbor (Figure 1F), suggesting that the PS membrane asymmetry is disrupted earlier at high-order branches than at lower-order branches. Kymographs for visualizing changes of dendrite morphology and AV-GFP binding over time (Figure 1G) further show that the appearance of AV-GFP signals (indicated by the blue dotted line) correlated with roughening of the dendritic membrane and occurred before dendrite fragmentation (indicated by the white dotted line). Both AV-GFP labeling and dendrite fragmentation proceeded from the distal end of the dendrite to the proximal end. These data suggest that PS exposure is among the early events of dendrite degeneration AI.

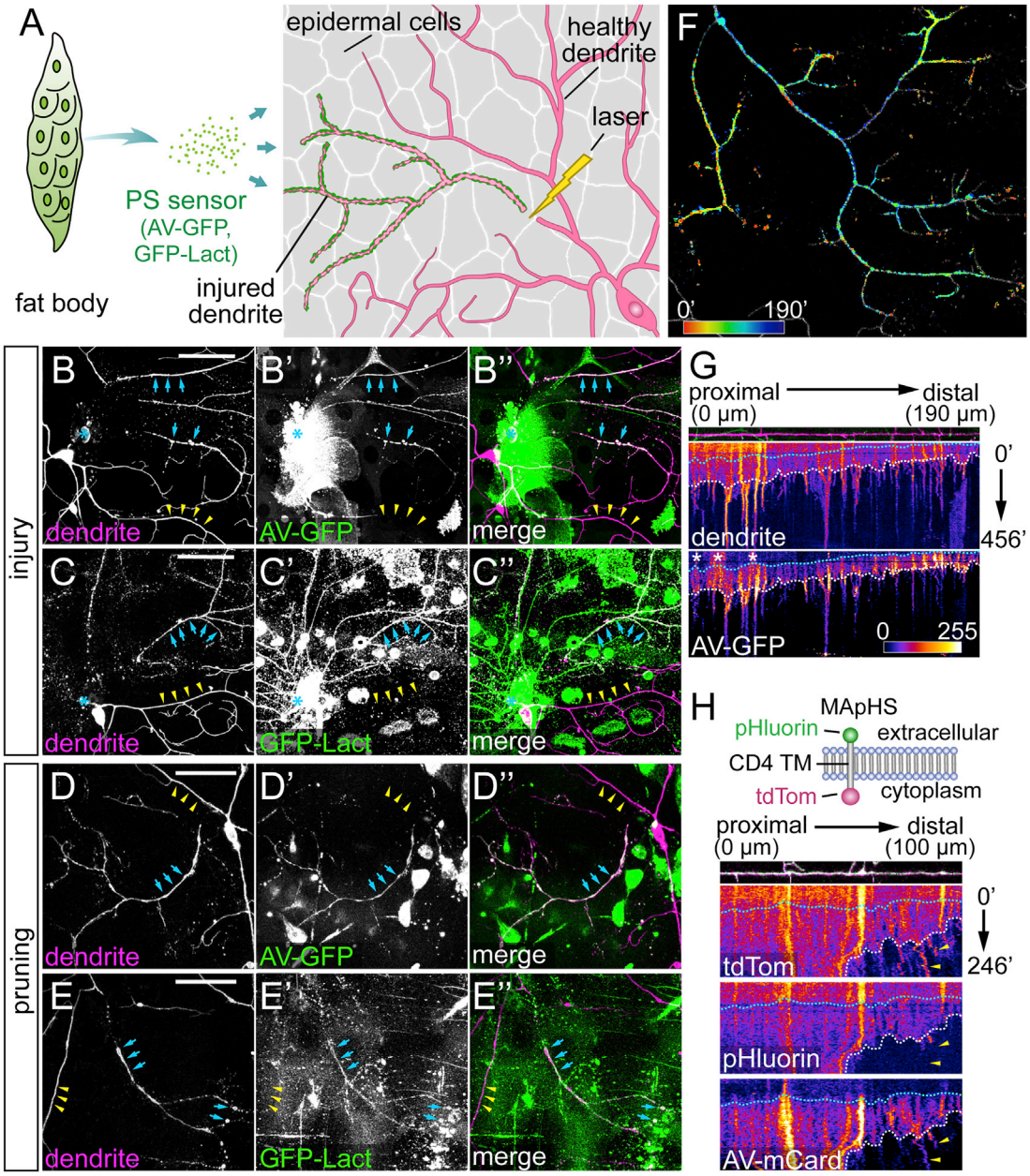

Figure 1. Phosphatidylserine Is Dynamically Exposed on Degenerating Dendrites after Injury and during Dendrite Remodeling

(A) Experimental design for visualizing PS exposure on injured dendrites of C4 da neurons.

(B–C″) Labeling of injured C4 da dendrites by AV-GFP (B–B″) and GFP-Lact (C–C″) at 4–5 hr after injury (AI). Blue arrows: injured dendrites; yellow arrowheads: uninjured dendrites; blue asterisk: injury sites.

(D–E″) Labeling of severed C4 da dendrites by AV-GFP (D–D″) and GFP-Lact (E–E″) during dendrite pruning between 6 and 7 hr after puparium formation (APF). Blue arrows: severed dendrites; yellow arrowheads: not-yet-severed dendrites. Some hemocytes are visible in the GFP channel in (B)–(D″) because *Dcg-Gal4* also drives expression in hemocytes.

(F) Temporal sequence of AV-GFP binding to injured dendrites (Video S3). Red: early binding; blue: late binding. Indicated times are relative to the first frame.

(G) Kymographs of morphology and AV-GFP binding of an injured dendrite. The top panel shows the straightened dendrite with indicated distances relative to the proximal (left) end. The middle and bottom panels show kymographs of tdTom and AV-GFP signals, respectively, with indicated times relative to the first frame. White dotted lines: timing of dendrite fragmentation based on the continuity of the dendrite signal; blue dotted lines: timing of AV-GFP initial binding to the dendrite; white asterisks: interfering AV-GFP signals from injured dendrites of other da neurons.

(H) Kymographs of engulfment and AV-mCard binding of an injured dendrite. Top panel: diagram of the MApHS marker (adapted from Han et al., 2011). Dendrite and kymograph panels are arranged similar to (G). White dotted lines: timing of dendrite fragmentation; blue dotted lines: timing of AV-mCard initial binding; yellow arrowheads: engulfed dendrite debris (based on the loss of pHluorin) still associated with AV-mCard.

Scale bars: 50 μm (B–E). See also Figure S1 and Videos S1, S2, S3, and S4.

To serve as an eat-me signal for degenerating dendrites, PS should be externalized before debris engulfment. Using MApHS, a pH sensitive dendritic marker consisting of extracellular pHluorin and intracellular tdTom (Han et al., 2014), to monitor engulfment and AV-mCardinal (AV-mCard) (Chu et al., 2014) to visualize PS exposure, we found that AV-mCard labeling (blue dotted line) appeared much earlier than engulfment (Figure 1H), which is signified by the loss of pHluorin signal due to the drop of pH in early phagosomes (Botelho and Grinstein, 2011) and mostly correlated with dendrite fragmentation (white dotted line). AV-mCard labeling can persist on dendrite debris even after engulfment (yellow arrowheads).

Together, our results demonstrate that PS is specifically and dynamically exposed on degenerating dendrites both in injury and during dendrite remodeling. The timing of PS exposure is consistent with its potential role as an eat-me signal.

PS Exposure on Injured Dendrites Depends on NAD^+ Depletion but Does Not Require Caspase Activity

Injured neurites degenerate following a sequence of signaling events triggered by NAD^+ depletion (Gerdts et al., 2016). Expression of Wld^S, a chimeric protein containing nicotinamide mononucleotide adenyltransferase (NMNAT1), which synthesizes NAD^+, in neurons prevents neurite degeneration AI (Mack et al., 2001). Interestingly, transected axons of retinal ganglion cells isolated from transgenic Wld^S rats showed a delay of PS exposure and halved the speed of PS exposure spread (Almasieh et al., 2017). To test whether PS exposure on injured dendrites is also regulated by NAD^+ depletion *in vivo*, we examined Wld^S-overexpressing C4 da neurons. At 10 hr AI, the majority of wild-type neurons showed complete fragmentation of injured dendrites, and the remaining dendrite segments were consistently labeled by GFP-Lact (Figures 2A–2A″ and 2E). In contrast, injured dendrites of Wld^S-overexpressing neurons showed little sign of fragmentation at 10 hr AI (Figures 2B–2B″ and 2E) or 24 hr AI. Neither did they show any GFP-Lact labeling (yellow arrowheads, Figure 2F), even though injured dendrites of other da neurons lacking Wld^S showed strong GFP-Lact labeling in the same segment (blue arrows). Occasionally (18%, n = 17), injured Wld^S-expressing dendrites broke into large segments that exhibited local enlargement and thinning without GFP-Lact labeling (Figures 2C–2C″, yellow arrowheads).

Caspase activity is involved in neurite pruning (Kuo et al., 2006; Schoenmann et al., 2010; Simon et al., 2012; Williams et al., 2006). During apoptosis, caspases inhibit P4-ATPases and activate XKR scramblases (Segawa and Nagata, 2015), and consequentially promote PS exposure. To test whether caspase activity is also required for PS exposure after dendrite injury, we expressed the caspase inhibitor p35 (Williams et al., 2006) in C4 da neurons. We did not observe statistically significant delay of dendrite degeneration (Figure 2E) or weaker GFP-Lact labeling on injured dendrites (Figures 2D–2F). Neurons overexpressing Diap1, a *Drosophila* inhibitor of caspases (Hay and Guo, 2006), showed normal degeneration and GFP-Lact labeling of injured dendrites (Figure 2E). Consistent with these results, caspase activity was not detected in injured dendrites of wild-type or p35-expressing neurons using a caspase activity reporter CD8::PARP::Venus (Williams et al., 2006) (Figure S2). Together, our results suggest that PS exposure on injured dendrites requires NAD^+ depletion, but not caspase activity.

CDC50 Knockout and TMEM16F Overexpression Disrupt PS Asymmetry Preferentially at Distal Dendrites

To understand the functional consequences of PS exposure, we sought to ectopically induce PS exposure on otherwise healthy neurons by removing P4-ATPases or overexpressing scramblases. The *Drosophila* genome encodes six P4-ATPases (Tanaka et al., 2011), five of which are predicted to require the chaperone CDC50 for proper subcellular localization and function (Paulusma et al., 2008; Saito et al., 2004; Tanaka et al., 2011). To maximize the chance of causing ectopic PS exposure, we knocked out the only *Drosophila CDC50* gene, *CG9947* (referred to as *CDC50* hereafter), in C4 da neurons using a C4 da-specific *ppk-Cas9* and two ubiquitously expressed guide RNAs (gRNAs) targeting *CDC50*. These *CDC50* mutant neurons were labeled by AV-GFP in bright puncta along high-order branches of distal dendrites (yellow arrowheads) and also smoothly on the shafts of low-order branches (blue arrows, Figures 3A–3A″). AV-GFP puncta appeared to be intracellular endosomes (Figures S3A–S3C″) and were also found in the cell body (Figures S3A–S3A″), possibly because of retrograde trafficking from dendrites. In contrast with AV-GFP, which did not seem to affect the morphology of *CDC50* knockout neurons, constitutive GFP-Lact expression in the fat body caused drastic dendrite degeneration of *CDC50* mutant neurons (more details later). To alleviate this degeneration, we transiently expressed GFP-Lact for 24 hr using temperature-sensitive Gal80 (McGuire et al., 2003), which resulted in varying degrees of GFP-Lact labeling on *CDC50* knockout neurons, with the strongest labeling typically seen at the most distal dendrites (Figure S3F). The GFP-Lact labeling was weak and smooth on dendrites without obvious sign of degeneration (Figures 3B–3B″, inset 1), whereas laser-injured dendrites of the same neurons exhibited much stronger GFP-Lact labeling (Figures 3B–3B″, inset 2), suggesting that loss of flippases causes low PS exposure preferentially at the distal dendritic arbor, and mechanisms other than P4-ATPase inactivation must exist to boost PS exposure AI.

We next overexpressed mammalian scramblases TMEM16F and XKR8 in da neurons. A hyperactive TMEM16F mutant, TMEM16F D430G-L (abbreviated as TMEM16F), causes a high level of ectopic PS exposure on mouse lymphoma cells (Segawa et al., 2011). TMEM16F overexpression in da neurons caused AV-mCard labeling in half of the neurons (50%, n = 12, 6 animals) (Figures 3C–3C″) in puncta in the cell body (inset 1) and on distal dendrites (inset 2). Constitutive GFP-Lact expression did not cause large-scale degeneration of TMEM16F-expressing neurons but labeled distal high-order branches infrequently (Figures 3D and 3E) and debris near distal dendrites frequently (Figures S3D and 3E). XKR8 overexpression did not cause obvious labeling by AV-GFP (data not shown) or GFP-Lact (Figures 3E and S3E).

We then asked whether combining *CDC50* knockout (KO) and TMEM16F overexpression (OE) (referred to as *CDC50* KO + TMEM16F OE) would enhance PS exposure by scoring GFP-Lact labeling (Figures S3F and S3H). Indeed, among neurons that showed GFP-Lact labeling, higher percentages of *CDC50*

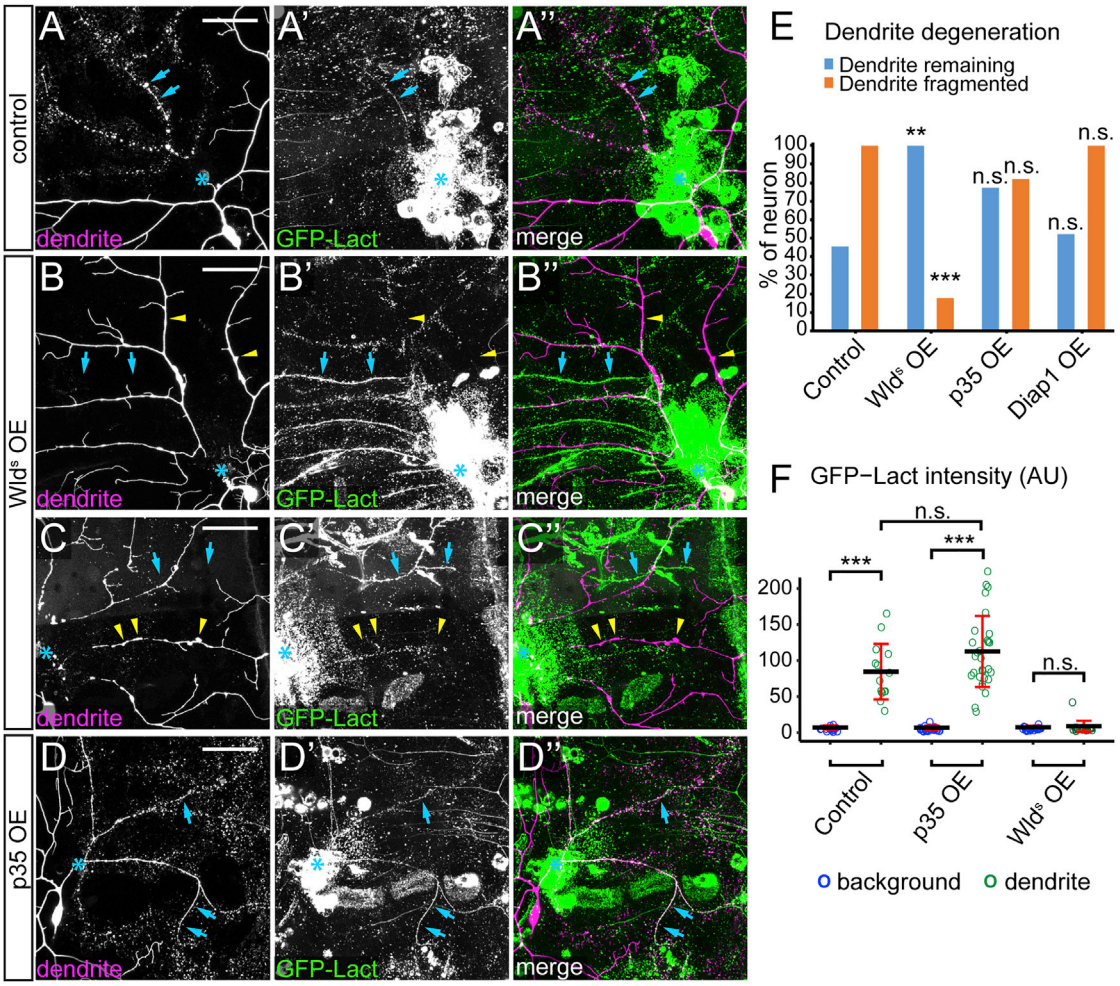

Figure 2. PS Exposure in Injured Dendrites Depends on NAD$^+$ Depletion but Does Not Require Caspase Activity

(A–A′′) A control C4 da neuron at 8–10 hr AI. Blue arrows: fragmenting dendrites.

(B–C′′) Wld^s-overexpressing (OE) C4 da neuron at 8–10 hr AI showing unfragmented dendrites (B–B′′) and fragmented dendrites (C–C′′). Yellow arrowheads: injured dendrites of C4 da neurons; blue arrows: injured dendrites of other classes of neurons that were labeled by GFP-Lact.

(D) A p35 OE neuron at 8–10 hr AI. Blue arrows: fragmenting dendrites.

(E) Quantification of dendrite degeneration showing percentages of neurons with uncleared dendrites and fragmented dendrites. n = number of neurons: control (n = 11, 7 animals); Wld^s OE (n = 17, 10 animals); p35 OE (n = 22, 11 animals); Diap1 OE (n = 21, 11 animals). Fisher's exact test, **p < 0.01; ***p < 0.001, n.s., not significant.

(F) Quantification of GFP-Lact binding on dendrites. GFP-Lact intensity is shown for both background epidermal regions and GFP-Lact-labeled dendrites. n = number of measurements: control (n = 15, 5 animals); p35 OE (n = 30, 9 animals), Wld^s OE (n = 24, 4 animals). ***p ≤ 0.001; n.s., not significant; Kruskal-Wallis (one-way ANOVA on ranks) and Dunn's test; p values adjusted with the Benjamini-Hochberg method. Black bar, mean; red bars, SD.

Scale bars represent 50 μm (A–D). Blue asterisks indicate injury sites (A–D). See also Figure S2.

KO + TMEM16F OE neurons (Figure S3G) were strongly labeled than *CDC50* KO alone (Figures 3F and S3F). Together, these data show that *CDC50* KO and TMEM16F OE induce different degrees of PS exposure preferentially at distal dendrites.

Ectopic PS Exposure in Neurons Causes Membrane Loss at Distal Dendrites

We next examined whether the low-level PS exposure on uninjured dendrites induced by flippase KO or scramblase OE would cause recognition and engulfment of dendrites by phagocytic epidermal cells, which would result in tdTom-positive phagosomes resembling dendrite debris (Han et al., 2014). When *CDC50* was knocked out in C4 da neurons, some dendrite debris was detected in epidermal cells underneath high-order dendrite branches (Figure 4B). To confirm that this phenotype is indeed caused by P4-ATPase loss of function (LOF), we knocked out *CG42321*, the closest *Drosophila* homolog for human 8A class of P4-ATPases (Tanaka et al., 2011) (referred to as *ATP8A* hereafter), in C4 da neurons and also detected dendrite debris in epidermal cells (Figures 4C and 4J). Knocking out both *CDC50* and *ATP8A* did not enhance debris formation (Figures 4D and 4J),

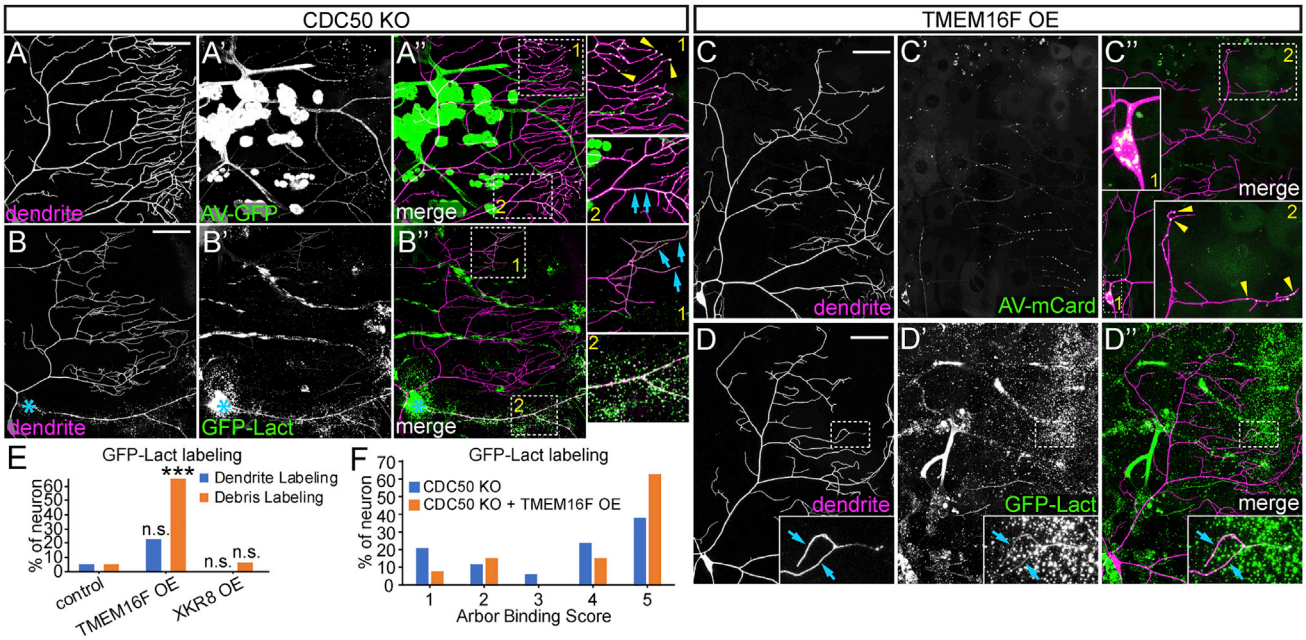

Figure 3. *CDC50* Knockout and TMEM16F Overexpression Disrupt PS Asymmetry Preferentially at Distal Dendrites

(A–A″) *CDC50* knockout (KO) neuron labeled by AV-GFP. Yellow arrowheads: bright AV-GFP puncta; blue arrows: smooth AV-GFP labeling on dendrite shafts.

(B–B″) *CDC50* KO neuron labeled by transiently induced GFP-Lact at 3–4 hr AI. Inset 1: weak, smooth labeling (blue arrows) on uninjured distal dendrites; inset 2: strong labeling on the injured dendrite; blue asterisks: injury sites.

(C–C″) TMEM16F OE neuron labeled by AV-mCard. Inset 1: AV-mCard in the cell body; inset 2: AV-mCard puncta along distal dendrites (yellow arrowheads).

(D–D″) TMEM16F OE neuron labeled by constitutively expressed GFP-Lact. Inset: smooth GFP-Lact labeling on distal dendrites (blue arrows).

(E) Percentage of neurons showing dendrite and debris labeling by constitutively expressed GFP-Lact. n = number of neurons: control (n = 20, 5 animals); TMEM16F OE (n = 31, 8 animals); XKR8 OE (n = 16, 4 animals). Fisher's exact test, ***p < 0.001. n.s., not significant.

(F) Arbor binding scores of GFP-Lact-labeled neurons. n = number of neurons: *CDC50* KO (n = 34, 10 animals, total neurons = 41); *CDC50* KO + TMEM16F OE (n = 27, 10 animals, total neurons = 45). Scoring system is illustrated in Figures S3F and S3H. Scale bars: 50 μm (A–D).

See also Figure S3.

consistent with the notion that ATP8A and CDC50 function in the same complex.

Whereas knocking out *CDC50* and *ATP8A* individually or in combination did not affect C4 da dendrite morphology (Figures S4A–S4D), TMEM16F OE caused a mild dendrite reduction (Figures S4E, S4J, and S4K). Consistent with their weaker PS-exposure phenotypes, TMEM16F-overexpressing neurons also produced a lower level of dendrite debris (Figures 4E and 4K). In contrast, XKR8 OE caused strong dendrite reduction (Figures S4H, S4J, and S4K) without generating dendrite debris (Figures 4K and S4N), suggesting that the dendrite reduction is due to dendrite growth defects rather than epidermal engulfment. Interestingly, *CDC50* KO + TMEM16F OE neurons showed a much greater level of debris than what would be expected from an additive effect of *CDC50* KO and TMEM16F overexpression (Figures 4F and 4K), suggesting that these two manipulations synergistically boost the loss of dendrite membranes. As a result, compared with TMEM16F OE alone, *CDC50* KO + TMEM16F OE neurons had fewer high-order dendrite branches (Figures S4F and S4J), even though arbor sizes were not affected (Figure S4K). In contrast, *CDC50* KO and XKR8 OE did not show synergistic effects on debris formation (Figures 4K and S4O) or dendrite reduction (Figure S4I, S4J, and S4K).

The scramblase activity of TMEM16F is activated by calcium. We asked whether increasing intracellular calcium levels by activating C4 da neurons would further enhance the membrane loss of *CDC50* KO + TMEM16F OE neurons. Because C4 da neurons respond to a variety of noxious stimuli including high temperatures (Hwang et al., 2007), we subjected larvae to brief heat shocks and examined C4 da neurons 30 min later. The heat shock treatment greatly increased the debris level (Figures 4I and 4L) and further reduced high-order dendrites (Figures S4G, S4J, and S4K) of *CDC50* KO + TMEM16F OE neurons but had no effect on wild-type neurons (Figures 4G and 4L). Interestingly, heat shocks did not affect TMEM16F OE alone (Figures 4H and 4L), suggesting that flippase loss is required for the enhancement effect of TMEM16F. Together, these data demonstrate that loss of P4-ATPase activity and TMEM16F activation in C4 da neurons synergistically causes engulfment of dendrite membrane by resident phagocytes.

Consistent with the preferential PS exposure at distal dendrites of *CDC50* KO and TMEM16F OE (Figure 3), dendrite debris also correlated with the distance from the cell body: the debris level is greater the farther away from the cell body and peaks near the edge of the dendritic field when normalized by either the number of all dendrite branches or that of terminal dendrites (Figure 4M). This spatial preference of membrane loss is not due

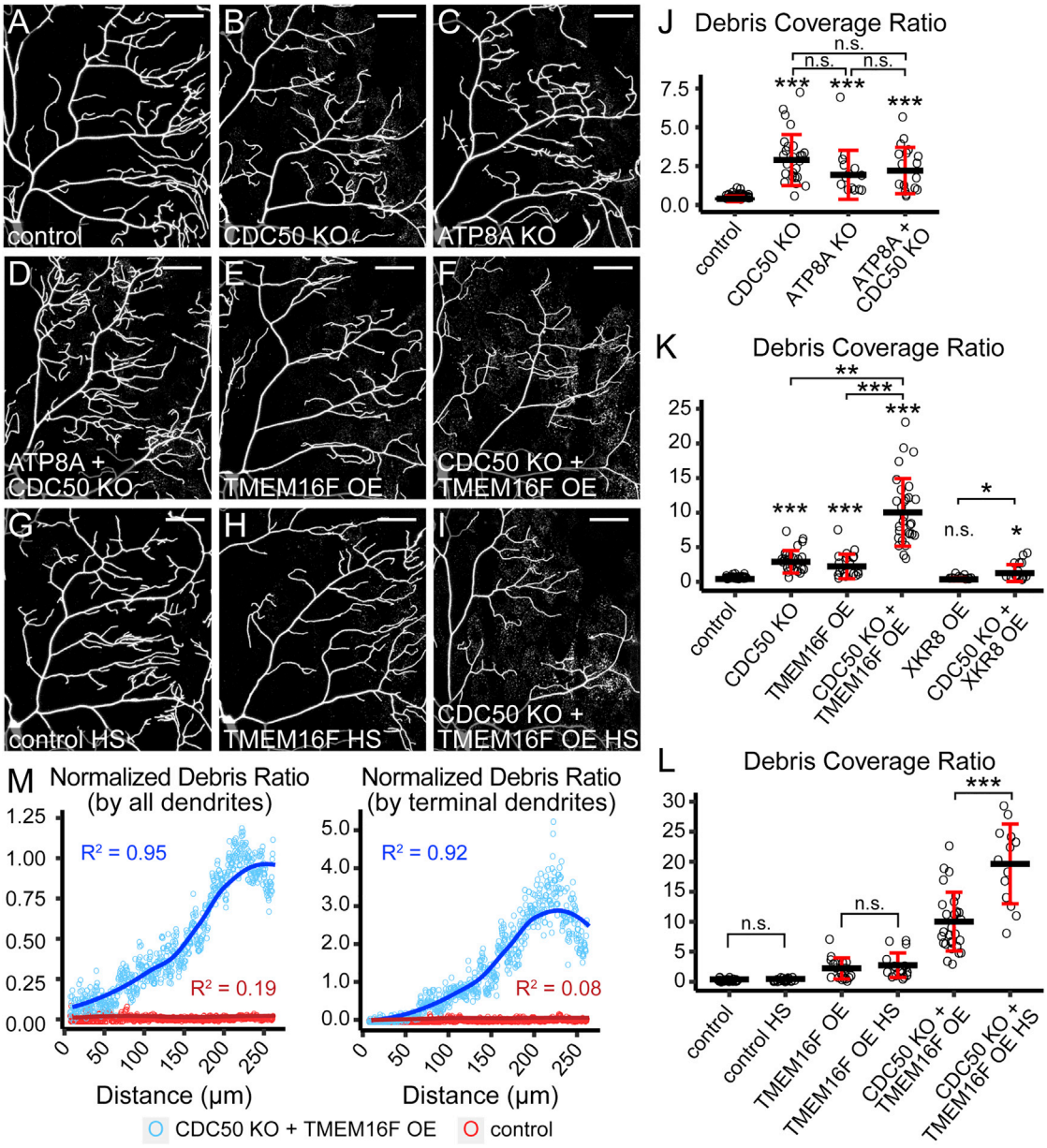

Figure 4. Ectopic PS Exposure in Neurons Causes Membrane Loss at Distal Dendrites

(A–F) Partial dendritic fields of control (A), *CDC50* KO (B), *ATP8A* KO (C), *ATP8A* and *CDC50* double KO (D), TMEM16F OE (E), and *CDC50* KO + TMEM16F OE (F) C4 da neurons.

(G–I) Partial dendritic fields of control (G), TMEM16F OE (H), and *CDC50* KO + TMEM16F OE (I) C4 da neurons after heat shock (HS) treatments.

(J and K) Quantification of debris coverage showing effects of flippase KO (J) and scramblase OE (K). The debris coverage ratio is debris area ratio normalized by dendrite area ratio. n = number of neurons: control (n = 35, 16 animals); *CDC50* KO (n = 25, 11 animals); *ATP8A* KO (n = 14, 9 animals); *ATP8A* + *CDC50* KO (n = 17, 9 animals); TMEM16F OE (n = 19, 9 animals); *CDC50* KO + TMEM16F OE (n = 29, 12 animals); XKR8 OE (n = 10, 8 animals); CDC50 KO + XKR8 OE (n = 16, 9 animals). *p ≤ 0.05, **p ≤ 0.01, ***p ≤ 0.001, Kruskal-Wallis (one-way ANOVA on ranks) and Dunn's test; p values adjusted with the Benjamini-Hochberg method.

(L) Quantification of debris coverage with or without heat shocks. n = number of neurons: control (n = 35, 16 animals); control HS (n = 23, 12 animals); TMEM16F OE (n = 19, 9 animals); TMEM16F OE HS (n = 18, 10 animals); CDC50 KO + TMEM16F OE (n = 29, 12 animals); *CDC50* KO + TMEM16F OE HS (n = 13, 7 animals). ***p ≤ 0.001, pairwise t test; p values adjusted with the Bonferroni method. n.s., not significant.

(M) Correlation between the debris ratio and the distance from the cell body in control (red) and *CDC50* KO + TMEM16F OE (blue). The average debris ratio at a given distance is average debris particle number divided by either total dendrite number (left panel) or terminal dendrite number (right panel). Circle: average debris ratio; solid line: polynomial fit of the average debris ratio; R^2: coefficient of determination of the linear regression. n = number of neurons: control (n = 35, 16 animals); *CDC50* KO + TMEM16F OE (n = 29, 12 animals).

Scale bars: 50 μm. Black bar: mean; red bars: SD. The control in (J)–(L) is the same dataset; *CDC50* KO in (J) and (K) is the same dataset; TMEM16F OE in (K) and (L) is the same dataset; *CDC50* KO + TMEM16F OE in (K) and (L) is the same dataset. See also Figure S4. n.s., not significant.

to TMEM16F enrichment at distal dendrites, because immunostaining showed that the TMEM16F protein was mostly found at the cell body and proximal dendrites (Figures S4L–S4L′′) and was below detection at distal high-order branches (Figures S4M–S4M′′). Together, these data suggested that distal dendrites of C4 da neurons are most susceptible to membrane loss due to perturbation of PS asymmetry caused by LOF of P4-ATPases or gain of function (GOF) of calcium-activated scramblases.

PS-Exposing Dendrites Shed Membrane Vesicles in a Phagocyte-Dependent Manner

To investigate how PS-exposing dendrites lose membranes, we conducted time-lapse imaging of *CDC50* KO + TMEM16F OE neurons and observed two ways by which dendrites shed membrane vesicles. More often, terminal dendrites shed vesicles from branch ends during retraction (Figure 5A; Video S5). Sometimes vesicles were shed from dendritic shafts (Figure 5B; Video S6), resembling the ''shedosomes'' emanated from dendritic shafts during dendrite pruning (Han et al., 2011). Both kinds of membrane shedding were rarely observed on wild-type neurons (Figure 5C), indicating that they are unique to PS-exposing dendrites. To ask whether PS exposure is sufficient to drive cell-autonomous membrane shedding, we examined animals mutant for *drpr*, which encodes an engulfment receptor necessary for larval epidermal cells to engulf dendrite debris (Han et al., 2014). We generated $drpr^{indel}$, a null allele, using CRISPR/Cas9. Strikingly, neither *CDC50* KO neurons (Figure 5E) nor CDC50 KO + TMEM16F OE neurons (Figure 5F) produced detectable debris in the $drpr^{indel}$ background, similar to control neurons in the $drpr^{indel}$ background (Figure 5D) or in wild-type animals (Figure 5G). These data suggest that vesicle shedding of PS-exposing dendrites results from Drpr-mediated attack and engulfment by epidermal cells on still live dendrites.

Mammalian macrophages have been reported to degrade unengulfed apoptotic cells by exocytosing lysosomal contents in a process called exophagy (Haka et al., 2016). To investigate whether epidermal cells also use similar mechanisms to acidify and degrade dendrite tips before separating them from the branches, we examined dendrite vesicle shedding with the MApHS marker. In all cases of vesicle shedding from dendrite tips (n = 77), the pHluorin signal persisted on the tips before shedding, and pHluorin quenching occurred at or shortly after the separation of vesicles from the branches (Figures 5H–5H′′ and 5I; Video S7), suggesting that epidermal cells do not acidify tips of terminal dendrites, and that epidermal cells may break dendrite tips by physical force (Han et al., 2014).

Flippase Loss and Scramblase OE Cause Distinct Modes of Axonal Degeneration in the Adult Fly Brain

We next asked whether flippase loss or scramblase OE could also cause neurons to lose axonal membrane in the CNS by examining adult Or22a neurons, which are a well-established model for studying axon degeneration and clearance in the brain (MacDonald et al., 2006). Or22a neurons are olfactory receptor neurons (ORNs) on the antenna that respond to ethyl butyrate and project axons to the DM2 glomeruli in the antennal lobe of the adult brain (Dobritsa et al., 2003). We knocked out *CDC50* in mature Or22a neurons labeled by *Or22a-Gal4 UAS-mCD8-GFP* to avoid potential early developmental defects. In 3-day-old adults, wild-type (Figure 6A) and *CDC50* KO (Figure 6B) neurons showed no differences in axonal GFP patterns and intensities (Figure 6E), whereas in 25-day-old adults, *CDC50* KO axons (Figures 6D, 6E, and S5F) showed much lower GFP than the wild-type (Figure 6C) and contained many GFP aggregates (inset of Figure 6D), indicating axonal degeneration.

To examine the effects of overexpressing TMEM16F in Or22a neurons, we compared 5-day-old flies exposed to ethyl butyrate with those not exposed to any odorant, all kept on sucrose agar to avoid potential exposure to odorants from the food, expecting that ethyl butyrate exposure would activate Or22a neurons and hence promote TMEM16F activity. In the absence of the odorant, TMEM16F OE slightly reduced axonal and somatic GFP signals (Figures 6G and S5A) compared with wild-type neurons (Figures 6F, 6J, and S5A). In the presence of the odorant, whereas wild-type neurons showed increased axonal and somatic GFP signals (Figures 6H, 6J, and S5B), TMEM16F-expressing neurons became fewer (Figures S5B) and their axons were largely missing except for few weak GFP-positive membrane blebs visible only under a much higher detection setting or by GFP staining (Figure 6I and S5C). The DM2 glomeruli in these TMEM16-expressing brains appeared to be much smaller and express much less the synaptic marker Brp (Figure S5C). These data suggest that activation of TMEM16F scramblase in adult ORNs causes strong axonal degeneration.

In comparison, odor exposure did not decrease axonal signals of *CDC50* KO neurons in 5-day-old flies (Figures 6J and S5D). Without odor exposure, TMEM16F-expressing axons did not degenerate with age: although they were much dimmer than controls in 3-day-old flies (Figures S5E and 6K), the signals increased rapidly in 5-day-old flies (Figures 6G and 6J) and further increased in 25-day-old flies (Figures S5E, S5F, and 6K). Interestingly, the somatic signals of TMEM16F-overexpressing neurons were comparable with those of the control in 3-day-old flies (Figure S5A), indicating a delay of axonal growth in young animals. Together, our results suggest that loss of P4-ATPase activity and TMEM16F OE causes distinct modes of axonal degeneration in ORNs: the former results in gradual and age-dependent axon degeneration, whereas the latter causes fast and neuronal activity-dependent axon degeneration.

The LactC1C2 Induces Engulfment-Dependent Dendritic Degeneration of PS-Exposing Neurons

Although *CDC50* KO C4 da neurons shed membrane at distal dendrites, their primary dendrites did not degenerate (Figures 7A–7A′′). Surprisingly, in the presence of constitutively expressed GFP-Lact, most *CDC50* KO neurons showed severe degeneration (Figures 7B–7B′′) and loss of high-order dendrites (Figure 7D), with membrane roughening and fragmentation on remaining branches. Strong GFP-Lact labeling was detected on dendrites and most cell bodies (14/20 neurons). *ATP8A* KO in C4 da neurons produced similar results in the presence of constitutively expressed GFP-Lact (Figures S6A–S6A′′), confirming that these phenotypes are related to the loss of P4-ATPase activity. To test whether GFP-Lact induces degeneration of PS-exposing neurons in the absence of epidermal phagocytic

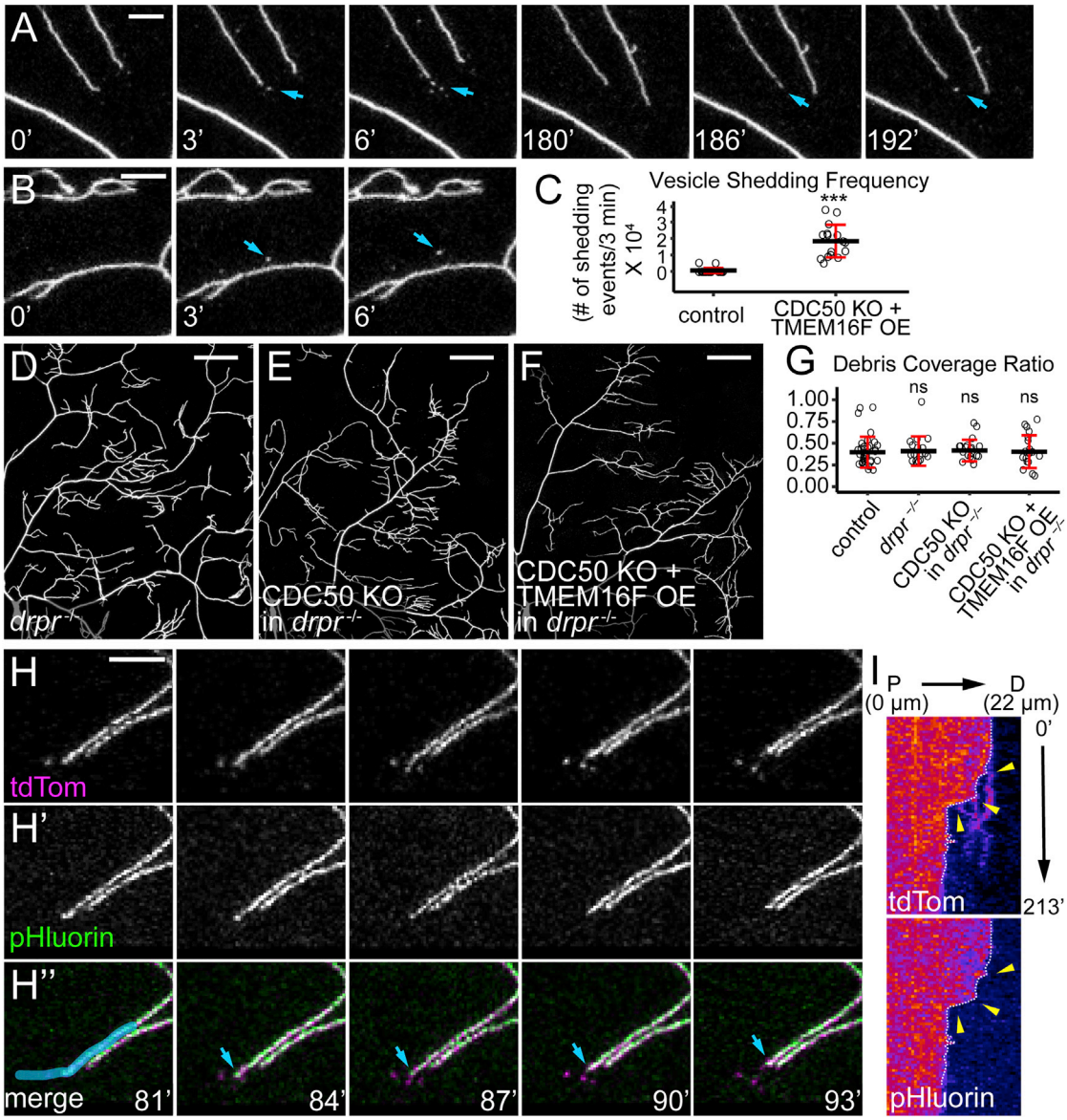

Figure 5. PS-Exposing Dendrites Shed Membrane Vesicles in a Phagocyte-Dependent Manner

(A and B) Time series of *CDC50* KO + TMEM16F OE dendrites showing vesicle shedding from a terminal branch (A) and a dendritic shaft (B). Indicated times are relative to the first frame.

(C) Vesicle shedding frequency defined as the number of shedding events per terminal dendrite in 3 min multiplied by 10^4. n = number of neurons: control (n = 21, 7 animals); *CDC50* KO +TMEM OE (n = 16, 5 animals). ***p $\leq$ 0.001, Kruskal-Wallis (one-way ANOVA on ranks) and Dunn's tests.

(D–F) Partial dendritic fields of control (D), *CDC50* KO (E), and *CDC50* KO + TMEM16F OE (F) neurons all in the $drpr^{-/-}$ background.

(G) Quantification of debris coverage. n = number of neurons: control (n = 35, 16 animals); $drpr^{-/-}$ (n = 17, 9 animals); *CDC50* KO in $drpr^{-/-}$ (n = 19, 11 animals); *CDC50* KO + TMEM16F OE in $drpr^{-/-}$ (n = 19, 9 animals). ANOVA, H_0 is true. n.s., not significant.

(H) A time series of *CDC50* KO + TMEM16F OE dendrites labeled by MApHS. Blue arrows: the tip of a vesicle-shedding terminal dendrite.

(I) Kymographs of membrane shedding and engulfment of the dendrite overlaid by blue color in (H''). White dotted lines: the tip of the dendrite in each frame; yellow arrowheads: vesicle shedding events.

Scale bars represent 10 μm (A, B, and H); 50 μm (D–F). Black bar: mean; red bars: SD (C and G). See also Videos S5, S6, and S7.

activity, we conducted similar experiments in the $drpr^{indel}$ background. Strikingly, $drpr^{indel}$ homozygosity completely rescued the degeneration and reduction of *CDC50* KO dendrites (Figures 7C and 7D), suggesting that GFP-Lact-induced degeneration is engulfment dependent. Consistent with the role of P4-ATPases, GFP-Lact was detected on distal dendrites of *CDC50* KO neurons in $drpr^{indel}$ (Figures 7E–7E''), albeit at a much lower level than that on *CDC50* KO neurons in the wild-type background (Figure 7F). Together, these data argue that GFP-Lact functions as a bridging molecule and potentiates phagocyte-dependent

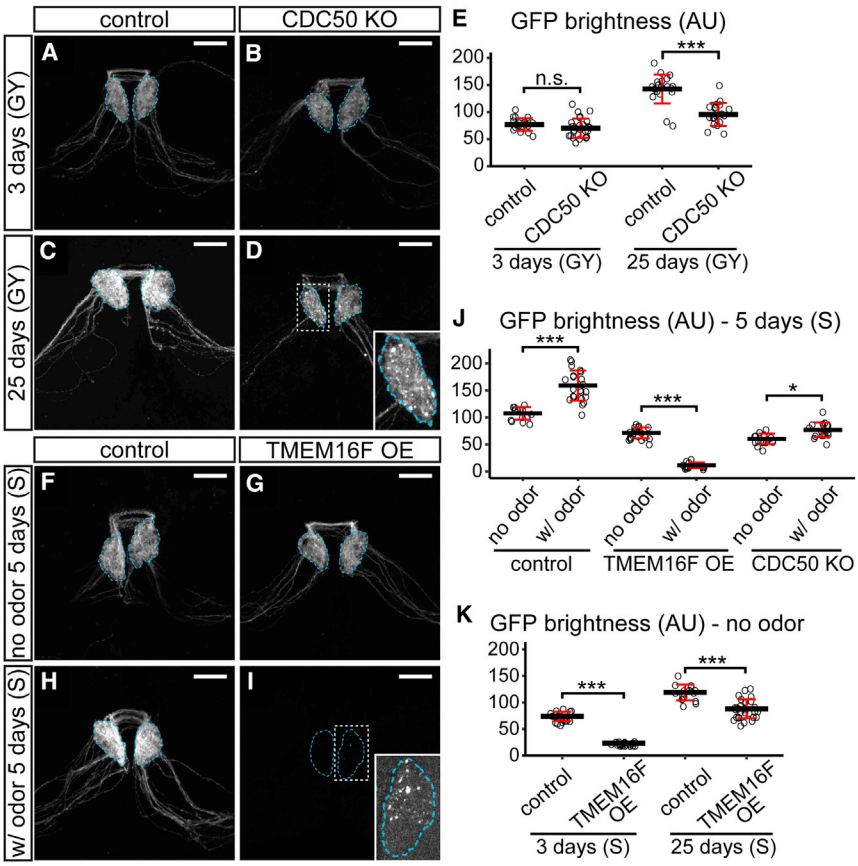

Figure 6. Flippase Loss and Scramblase Overexpression Cause Distinct Modes of Axonal Degeneration in the Adult Fly Brain

(A–D) Axons of control (A) and *CDC50* KO (B) Or22a neurons in 3-day-old adult brains and axons of control (C) and CDC50 KO (D) OR22a neurons in 25-day-old brains. The inset in (D) is an enlarged glomerulus.

(E) Quantification of GFP brightness of Or22a glomeruli in age tests. n = number of brains: control 3 days (n = 19); CDC50 KO 3 days (n = 26); control 25 days (n = 21); *CDC50* KO 25 days (n = 19). ***p ≤ 0.001, one-way ANOVA and Tukey's HSD. n.s., not significant.

(F–I) Axons of control (F) and TMEM16F OE (G) Or22a neurons in 5-day-old adult flies that were not exposed to the odor and control (H) and TMEM16F OE (I) axons in flies that were exposed to the odor. The inset in (I) is an enlarged glomerulus imaged at a much brighter setting.

(J) Quantification of GFP brightness in odor tests. n = number of brains: control no odor (n = 14); control with (w/) odor (n = 22); TMEM16F OE no odor (n = 21); TMEM16F OE w/ odor (n = 16); *CDC50* KO no odor (n = 16); *CDC50* KO w/ odor (n = 18). *p ≤ 0.05; ***p ≤ 0.001, one-way ANOVA and Tukey's HSD test.

(K) Quantification of GFP brightness in age tests. n = number of brains: control 3 days (n = 20); TMEM16F OE3 days (n = 21); control 25 days (n = 16); TMEM16F OE 25 days (n = 29). ***p ≤ 0.001, one-way ANOVA and Tukey's HSD.

In all image panels, Or22a glomeruli are outlined. The types of food used are indicated for each panel: GY, glucose yeast medium; S, sucrose agar. Scale bars: 20 μm. Black bars: mean; red bars: SD. See also Figure S5.

destruction of dendrites exposing low levels of PS. Our results also suggest that the LactC1C2 domain contains an unidentified sequence that can interact with a *Drosophila* engulfment receptor, perhaps Drpr.

DISCUSSION

PS Exposure Is Associated with Neurite Degeneration

Our results demonstrate that externalized PS is associated with neurite degeneration in two ways. First, PS exposure results from neurite degeneration (Figure S7A). Both pruned dendrites during developmental remodeling and severed dendrites after physical injury dynamically expose PS. The onset of PS exposure coincides with early signs of dendrite degeneration such as membrane roughening and blebbing, but precedes dendrite fragmentation and engulfment. Moreover, PS exposure is blocked when degeneration of injured dendrites is inhibited by Wld^S expression, suggesting that PS exposure is a downstream event of the neurite degeneration program triggered by NAD^+ depletion (Almasieh et al., 2017; Gerdts et al., 2016). Interestingly, PS exposure in injured dendrites does not depend on caspase activity, consistent with previous findings that blocking caspase activity does not protect dendrites or axons from injury-induced degeneration (Simon et al., 2012; Tao and Rolls, 2011).

Second, ectopic PS exposure on neurites causes phagocyte-dependent membrane loss (Figure S7B). Flippase KO or TMEM16F OE led to PS exposure preferentially on distal high-order dendrites of C4 da neurons and, consequently, membrane shedding from PS-exposing dendrites. This kind of membrane loss in severe cases (such as in *CDC50* KO + TMEM16F OE neurons) can lead to strong dendrite reduction. In the CNS, *CDC50* KO and TMEM16F OE in adult olfactory neurons also caused age-dependent and neuronal activity-dependent axon degeneration, respectively. Although PS exposure is associated with cell-autonomous membrane vesicle shedding in apoptosis (Frey and Gaipl, 2011), necroptosis (Gong et al., 2017), tumor cell microvesicle formation (Lima et al., 2009; Muralidharan-Chari et al., 2009), and cell membrane repair (Scheffer et al., 2014), in the context of da neurons, PS-exposure by itself does not cause vesicle shedding, because membrane loss of PS-exposing dendrites is completely blocked in the *drpr* mutant background. Instead, epidermal cells likely latch on PS-exposing dendritic tips and cause them to separate as dendrites retract. In the CNS, glia may also actively damage PS-exposing axons through phagocytosis (Freeman, 2015). Together, our results establish a strong association between PS exposure and neurite degeneration, and argue that PS exposure is sufficient to cause phagocyte-dependent neurite degeneration.

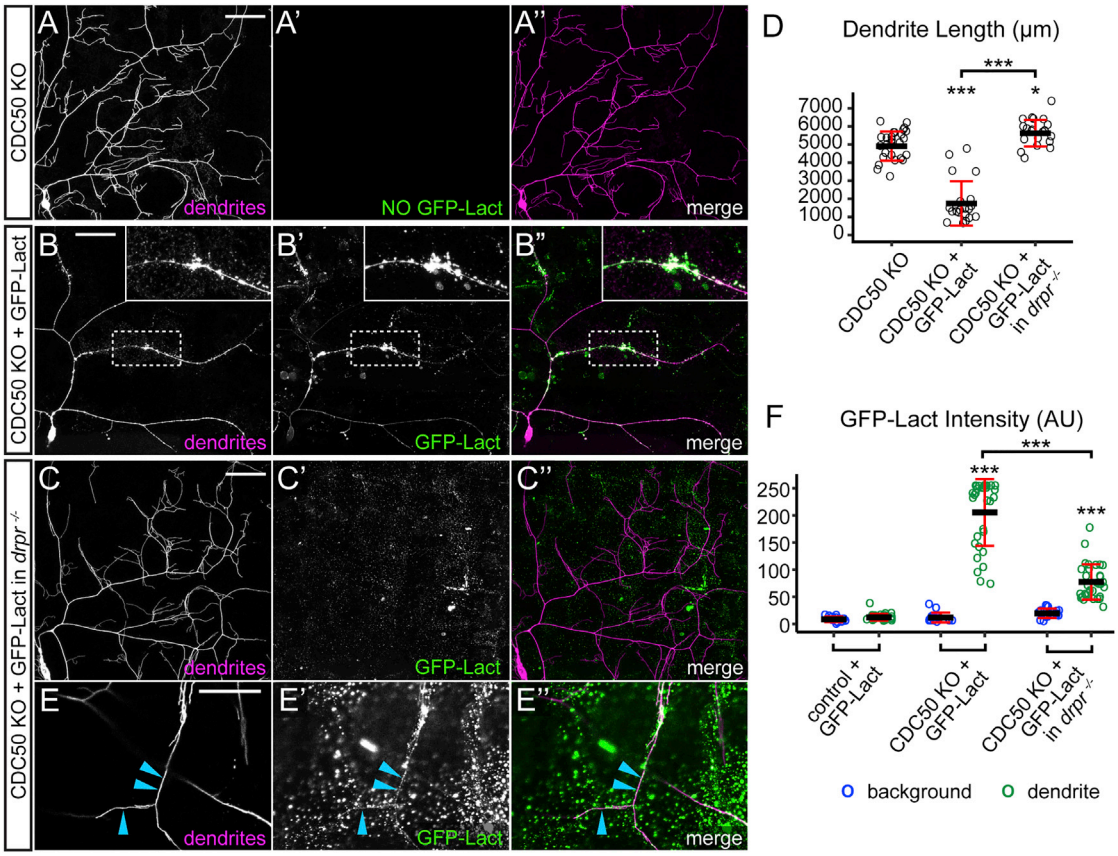

Figure 7. The Lactadherin C1C2 Domain Induces Engulfment-Dependent Dendritic Degeneration of PS-Exposing Neurons

(A–C′′) Partial dendritic fields of CDC50 KO neurons in the absence (A–A′′) and presence (B–B′′) of constitutive GFP-Lact expression. Inset in (B)–(B′′): a segment of degenerating dendrite strongly labeled by GFP-Lact.

(C–C′′) Partial dendritic fields of CDC50 KO neurons in *drpr*$^{-/-}$ background in the presence of constitutive GFP-Lact expression.

(D) Dendrite length in the partial ddaC dendritic field. n = number of neurons: *CDC50* KO (n = 27, 9 animals); *CDC50* KO + GFP-Lact (n = 20, 9 animals); *CDC50* KO + GFP-Lact in *drpr*$^{-/-}$ (n = 21, 9 animals). *p ≤ 0.05; ***p ≤ 0.001, one-way ANOVA and Tukey's HSD test.

(E–E′′) High-resolution images of *CDC50* KO distal dendrites in the presence of constitutively expressed GFP-Lact in *drpr*$^{-/-}$ background taken at a brighter GFP setting. Maximum projection of two Z slices covering 2-μm-thick volume. Blue arrows: GFP-Lact labeling on dendrites.

(F) Quantification of GFP-Lact binding on dendrites. Background: epidermal regions without dendrites. n = number of measurements: control background (n = 14) and control dendrite (n = 28), 7 animals; *CDC50* KO + GFP-Lact background (n = 16) and *CDC50* KO + GFP-Lact dendrite (n = 32), 8 animals; *CDC50* KO + GFP-Lact in *drpr*$^{-/-}$ background (n = 16) and *CDC50* KO + GFP-Lact in *drpr*$^{-/-}$ dendrite (n = 32), 5 animals. ***p ≤ 0.001, Kruskal-Wallis (one-way ANOVA on ranks) and Dunn's test; p values adjusted with the Benjamini-Hochberg method.

Black bars: mean; red bars: SD. See also Figure S6.

Different Spatial Domains of Neurons Are Differentially Sensitive to the Perturbation of PS Asymmetry

Our results reveal that distal dendritic arbors of C4 da neurons are most vulnerable to disruption of PS asymmetry. Ectopically externalized PS appeared preferentially on distal high-order branches where the phagocyte-dependent neuronal membrane loss was the most severe. These results suggest that different spatial domains of the same dendritic arbor have different demands for maintaining PS asymmetry. One possibility for such spatial differences is that distal dendrites are more active in certain cellular activities that could cause PS externalization. Such activities may include calcium influx and stimulation of calcium-dependent scramblases, endocytosis, and exocytosis in inducing phospholipid scrambling (Janmey and Kinnunen, 2006), and the generation of oxidative stress (de Jong and Kuypers, 2006). Mechanistically, this differential sensitivity to PS asymmetry disruption is likely different from the diurnal and spatially restricted PS exposure on mammalian POS tips (Ruggiero et al., 2012), because the latter is a constant, physiological, and tightly regulated process that involves coordination between the neurons and their specialized phagocytes.

The Effects of Flippase LOF and Scramblase GOF Depends on the Cellular Context

Interestingly, flippase LOF and scramblase GOF produced distinct modes of degeneration that differ between larval C4 da dendrites and adult Or22a axons. These outcomes might be explained by the kinetics of PS externalization. The absence of P4-ATPase activity may lead to slow and cumulative PS externalization, which could explain the age dependency of Or22a axon

degeneration and the weak phenotype of larval C4 da neurons (considering the relatively short larval period). In contrast, the effect of TMEM16F, which can cause a more rapid PS exposure, is likely controlled by local calcium influx. In nociceptive C4 da neurons, short bursts of TMEM16F activity likely only cause local and transient PS exposure as endogenous flippases reestablish PS asymmetry. In contrast, sustained and strong TMEM16F activity, such as in activated Or22a neurons, may override the effect of endogenous flippases, leading to massive PS exposure and severe neurite degeneration. Lastly, when TMEM16F is overexpressed in *CDC50* KO neurons, the lack of flippase activity may unmask the full effect of TMEM16F, which could underlie the synergistic effects of *CDC50* KO and TMEM16 OE. Although other indirect effects of *CDC50* KO and TMEM16F OE cannot be ruled out, our results highlight the importance of the cellular context in determining the outcome of ectopic PS exposure.

A Potential Bridging Function of the LactC1C2 Domain

We found that prolonged exposure to GFP-Lact caused PS-exposing dendrites to degenerate in a phagocyte-dependent manner. This is a surprising result because the RGD motif required for lactadherin interaction with mammalian integrin receptors (Hanayama et al., 2002; Mapes et al., 2012) is missing in LactC1C2 used to construct GFP-Lact. LactC1C2 may contain a yet unidentified sequence that can interact with other engulfment receptors. In comparison, AV appears to be a more passive PS-binding protein: AV did not affect the clearance of the degenerating dendrites or cause degeneration of *CDC50* KO neurons, but was often located in intracellular vesicles in PS-exposing neurons, likely a result of endocytosis.

Potential Roles of PS Exposure in Neurodevelopment and Neurodegenerative Diseases

Trimming of unnecessary neuronal branches or neuronal connections is an important step in the assembly of functional neural circuits (Chung et al., 2015; Schuldiner and Yaron, 2015). Our results suggest that PS exposure plays an important role in phagocytic recognition and clearance of pruned C4 da dendrites. It will be interesting to examine whether PS exposure also marks processes or synapses for elimination in other contexts of neurite and synaptic pruning. Furthermore, in neurodegenerative diseases, neurons can lose dendrites and axonal branches well before they die. Our results demonstrate that improper PS exposure in living neurons can cause neurite loss. Therefore, it is important to fully investigate whether and how spatial and temporal disruption of PS asymmetry on neurons relates to neurodegenerative pathologies.

EXPERIMENTAL PROCEDURES

Live Imaging and Dendrite Ablation

Animals were reared at 25°C in density-controlled vials. Larvae at 125 hr after legg laying (AEL) (wandering stage) were imaged using a Leica SP8 microscope. Unless stated otherwise, confocal images shown in all figures are maximum intensity projections of z stacks encompassing the epidermal layer and the sensory neurons beneath, which are typically 8–10 μm for larvae and 12–15 μm for pupae. For dendrite lesion, laser ablation was performed on a Zeiss LSM880 Confocal/Multiphoton Upright Microscope, using a 790-nm two-photon laser at primary dendrites of ddaC neurons in A1 and A3 segments at 90 hr AEL. Animals were recovered on grape juice agar plates following lesion for appropriate time. After recovery, the larvae were imaged using a Leica SP8 microscope. Long-term time-lapse imaging at the larval stage was done as described previously (Poe et al., 2017) with small modifications. For long-term time-lapse imaging of dendrite pruning, white pupae were directly mounted in the imaging chamber similar to larval mounting and kept on the imaging chamber for 4–6 hr before imaging.

Quantification and Statistical Analysis

Data acquisition and quantification were performed non-blinded in ImageJ and Microsoft Excel, respectively. Statistical significance was determined using one-way ANOVA and Tukey's honest significant difference (HSD) or Kruskal-Wallis (one-way ANOVA on ranks) and Dunn's test in R (*$p < 0.05$; **$p < 0.01$; ***$p < 0.001$). Statistical significance was set at $p < 0.05$.

The detailed descriptions for *Drosophila* stocks, molecular cloning and transgenic flies, generation of $drpr^{indel}$ allele by CRISPR/Cas9, tissue-specific gene KO via CRISPR/Cas9, adult brain preparation and adult odor treatment, immunohistochemistry, heat shock conditions, live imaging and long-term time-lapse imaging, image analysis, and quantification can be found in the Supplemental Experimental Procedures.

SUPPLEMENTAL INFORMATION

Supplemental Information includes Supplemental Experimental Procedures, seven figures, and seven videos and can be found with this article online at https://doi.org/10.1016/j.celrep.2018.07.095.

ACKNOWLEDGMENTS

We thank Marc Freeman, Yang Xiang, Jon Graff, and Bloomington Stock Center for fly stocks; Ding Xue, Shigekazu Nagata, Thomas Kornberg, and Addgene for plasmids; Yalei Wu for cloning and immunochemistry reagents; Halocarbon Products Corporation for Halocarbon oils; Cornell BRC Imaging facility for access to microscopes (funded by National Institutes of Health (NIH), United States, grant S10OD018516); and Scott Emr, Mariana Wolfner, Joe Fetcho, Chris Fromme, Michael Goldberg, Fenghua Hu, and Felicity Emerson for critical reading and suggestions on the manuscript. This work was supported by a Cornell Fellowship awarded to H.J., and a Cornell start-up fund and NIH grants (R01NS099125 and R21OD023824) awarded to C.H.

AUTHOR CONTRIBUTIONS

Conceptualization, C.H., M.L.S., and H.J.; Methodology, C.H., M.L.S., and H.J.; Investigation, C.H., M.L.S., H.J., K.D., and A.R.P.; Software, C.H. and K.D.; Formal Analysis, M.L.S., H.J., and K.D.; Resources, C.H., M.L.S., H.J., B.W., X.R., and J.-Q.N.; Writing – Original Draft, C.H., M.L.S., and H.J.; Writing – Review and Editing, C.H., M.L.S., and H.J.; Funding Acquisition, C.H. and H.J.

DECLARATION OF INTERESTS

The authors declare no competing interests.

Received: November 15, 2017
Revised: May 25, 2018
Accepted: July 27, 2018
Published: August 28, 2018

REFERENCES

Almasieh, M., Catrinescu, M.M., Binan, L., Costantino, S., and Levin, L.A. (2017). Axonal degeneration in retinal ganglion cells is associated with a membrane polarity-sensitive redox process. J. Neurosci. *37*, 3824–3839.

Andersen, M.H., Graversen, H., Fedosov, S.N., Petersen, T.E., and Rasmussen, J.T. (2000). Functional analyses of two cellular binding domains of bovine lactadherin. Biochemistry *39*, 6200–6206.

Appelt, U., Sheriff, A., Gaipl, U.S., Kalden, J.R., Voll, R.E., and Herrmann, M. (2005). Viable, apoptotic and necrotic monocytes expose phosphatidylserine: cooperative binding of the ligand Annexin V to dying but not viable cells and implications for PS-dependent clearance. Cell Death Differ. *12*, 194–196.

Botelho, R.J., and Grinstein, S. (2011). Phagocytosis. Curr. Biol. *21*, R533–R538.

Brown, G.C., and Neher, J.J. (2014). Microglial phagocytosis of live neurons. Nat. Rev. Neurosci. *15*, 209–216.

Chu, J., Haynes, R.D., Corbel, S.Y., Li, P., González-González, E., Burg, J.S., Ataie, N.J., Lam, A.J., Cranfill, P.J., Baird, M.A., et al. (2014). Non-invasive intravital imaging of cellular differentiation with a bright red-excitable fluorescent protein. Nat. Methods *11*, 572–578.

Chung, W.S., Welsh, C.A., Barres, B.A., and Stevens, B. (2015). Do glia drive synaptic and cognitive impairment in disease? Nat. Neurosci. *18*, 1539–1545.

de Jong, K., and Kuypers, F.A. (2006). Sulphydryl modifications alter scramblase activity in murine sickle cell disease. Br. J. Haematol. *133*, 427–432.

Dobritsa, A.A., van der Goes van Naters, W., Warr, C.G., Steinbrecht, R.A., and Carlson, J.R. (2003). Integrating the molecular and cellular basis of odor coding in the Drosophila antenna. Neuron *37*, 827–841.

Dubois, T., Mira, J.P., Feliers, D., Solito, E., Russo-Marie, F., and Oudinet, J.P. (1998). Annexin V inhibits protein kinase C activity via a mechanism of phospholipid sequestration. Biochem. J. *330*, 1277–1282.

Emoto, K. (2011). Dendrite remodeling in development and disease. Dev. Growth Differ. *53*, 277–286.

Fourgeaud, L., Través, P.G., Tufail, Y., Leal-Bailey, H., Lew, E.D., Burrola, P.G., Callaway, P., Zagórska, A., Rothlin, C.V., Nimmerjahn, A., and Lemke, G. (2016). TAM receptors regulate multiple features of microglial physiology. Nature *532*, 240–244.

Freeman, M.R. (2015). Drosophila central nervous system glia. Cold Spring Harb. Perspect. Biol. *7*, a020552.

Frey, B., and Gaipl, U.S. (2011). The immune functions of phosphatidylserine in membranes of dying cells and microvesicles. Semin. Immunopathol. *33*, 497–516.

Fricker, M., Neher, J.J., Zhao, J.W., Théry, C., Tolkovsky, A.M., and Brown, G.C. (2012). MFG-E8 mediates primary phagocytosis of viable neurons during neuroinflammation. J. Neurosci. *32*, 2657–2666.

Fujii, T., Sakata, A., Nishimura, S., Eto, K., and Nagata, S. (2015). TMEM16F is required for phosphatidylserine exposure and microparticle release in activated mouse platelets. Proc. Natl. Acad. Sci. USA *112*, 12800–12805.

Gerdts, J., Summers, D.W., Milbrandt, J., and DiAntonio, A. (2016). Axon self-destruction: new links among SARM1, MAPKs, and NAD+ metabolism. Neuron *89*, 449–460.

Gong, Y.N., Guy, C., Olauson, H., Becker, J.U., Yang, M., Fitzgerald, P., Linkermann, A., and Green, D.R. (2017). ESCRT-III acts downstream of MLKL to regulate necroptotic cell death and its consequences. Cell *169*, 286–300.e216.

Grueber, W.B., Jan, L.Y., and Jan, Y.N. (2002). Tiling of the Drosophila epidermis by multidendritic sensory neurons. Development *129*, 2867–2878.

Haka, A.S., Barbosa-Lorenzi, V.C., Lee, H.J., Falcone, D.J., Hudis, C.A., Dannenberg, A.J., and Maxfield, F.R. (2016). Exocytosis of macrophage lysosomes leads to digestion of apoptotic adipocytes and foam cell formation. J. Lipid Res. *57*, 980–992.

Han, C., Jan, L.Y., and Jan, Y.N. (2011). Enhancer-driven membrane markers for analysis of nonautonomous mechanisms reveal neuron-glia interactions in Drosophila. Proc. Natl. Acad. Sci. USA *108*, 9673–9678.

Han, C., Wang, D., Soba, P., Zhu, S., Lin, X., Jan, L.Y., and Jan, Y.N. (2012). Integrins regulate repulsion-mediated dendritic patterning of Drosophila sensory neurons by restricting dendrites in a 2D space. Neuron *73*, 64–78.

Han, C., Song, Y., Xiao, H., Wang, D., Franc, N.C., Jan, L.Y., and Jan, Y.N. (2014). Epidermal cells are the primary phagocytes in the fragmentation and clearance of degenerating dendrites in Drosophila. Neuron *81*, 544–560.

Hanayama, R., Tanaka, M., Miwa, K., Shinohara, A., Iwamatsu, A., and Nagata, S. (2002). Identification of a factor that links apoptotic cells to phagocytes. Nature *417*, 182–187.

Hay, B.A., and Guo, M. (2006). Caspase-dependent cell death in Drosophila. Annu. Rev. Cell Dev. Biol. *22*, 623–650.

Heemskerk, J.W., Bevers, E.M., and Lindhout, T. (2002). Platelet activation and blood coagulation. Thromb. Haemost. *88*, 186–193.

Hwang, R.Y., Zhong, L., Xu, Y., Johnson, T., Zhang, F., Deisseroth, K., and Tracey, W.D. (2007). Nociceptive neurons protect Drosophila larvae from parasitoid wasps. Curr. Biol. *17*, 2105–2116.

Janmey, P.A., and Kinnunen, P.K. (2006). Biophysical properties of lipids and dynamic membranes. Trends Cell Biol. *16*, 538–546.

Kanamori, T., Kanai, M.I., Dairyo, Y., Yasunaga, K., Morikawa, R.K., and Emoto, K. (2013). Compartmentalized calcium transients trigger dendrite pruning in Drosophila sensory neurons. Science *340*, 1475–1478.

Kim, Y.E., Chen, J., Chan, J.R., and Langen, R. (2010). Engineering a polarity-sensitive biosensor for time-lapse imaging of apoptotic processes and degeneration. Nat. Methods *7*, 67–73.

Kim, M.E., Shrestha, B.R., Blazeski, R., Mason, C.A., and Grueber, W.B. (2012). Integrins establish dendrite-substrate relationships that promote dendritic self-avoidance and patterning in Drosophila sensory neurons. Neuron *73*, 79–91.

Koopman, G., Reutelingsperger, C.P., Kuijten, G.A., Keehnen, R.M., Pals, S.T., and van Oers, M.H. (1994). Annexin V for flow cytometric detection of phosphatidylserine expression on B cells undergoing apoptosis. Blood *84*, 1415–1420.

Kuo, C.T., Zhu, S., Younger, S., Jan, L.Y., and Jan, Y.N. (2006). Identification of E2/E3 ubiquitinating enzymes and caspase activity regulating Drosophila sensory neuron dendrite pruning. Neuron *51*, 283–290.

Lemke, G. (2013). Biology of the TAM receptors. Cold Spring Harb. Perspect. Biol. *5*, a009076.

Lew, E.D., Oh, J., Burrola, P.G., Lax, I., Zagórska, A., Través, P.G., Schlessinger, J., and Lemke, G. (2014). Differential TAM receptor-ligand-phospholipid interactions delimit differential TAM bioactivities. eLife *3*, e03385.

Lima, L.G., Chammas, R., Monteiro, R.Q., Moreira, M.E., and Barcinski, M.A. (2009). Tumor-derived microvesicles modulate the establishment of metastatic melanoma in a phosphatidylserine-dependent manner. Cancer Lett. *283*, 168–175.

Lin, L., Huai, Q., Huang, M., Furie, B., and Furie, B.C. (2007). Crystal structure of the bovine lactadherin C2 domain, a membrane binding motif, shows similarity to the C2 domains of factor V and factor VIII. J. Mol. Biol. *371*, 717–724.

Luo, L., and O'Leary, D.D. (2005). Axon retraction and degeneration in development and disease. Annu. Rev. Neurosci. *28*, 127–156.

MacDonald, J.M., Beach, M.G., Porpiglia, E., Sheehan, A.E., Watts, R.J., and Freeman, M.R. (2006). The Drosophila cell corpse engulfment receptor Draper mediates glial clearance of severed axons. Neuron *50*, 869–881.

Mack, T.G., Reiner, M., Beirowski, B., Mi, W., Emanuelli, M., Wagner, D., Thomson, D., Gillingwater, T., Court, F., Conforti, L., et al. (2001). Wallerian degeneration of injured axons and synapses is delayed by a Ube4b/Nmnat chimeric gene. Nat. Neurosci. *4*, 1199–1206.

Mapes, J., Chen, Y.Z., Kim, A., Mitani, S., Kang, B.H., and Xue, D. (2012). CED-1, CED-7, and TTR-52 regulate surface phosphatidylserine expression on apoptotic and phagocytic cells. Curr. Biol. *22*, 1267–1275.

McGuire, S.E., Le, P.T., Osborn, A.J., Matsumoto, K., and Davis, R.L. (2003). Spatiotemporal rescue of memory dysfunction in Drosophila. Science *302*, 1765–1768.

Morel, O., Toti, F., Hugel, B., and Freyssinet, J.M. (2004). Cellular microparticles: a disseminated storage pool of bioactive vascular effectors. Curr. Opin. Hematol. *11*, 156–164.

Muralidharan-Chari, V., Clancy, J., Plou, C., Romao, M., Chavrier, P., Raposo, G., and D'Souza-Schorey, C. (2009). ARF6-regulated shedding of tumor cell-derived plasma membrane microvesicles. Curr. Biol. *19*, 1875–1885.

Naftelberg, S., Abramovitch, Z., Gluska, S., Yannai, S., Joshi, Y., Donyo, M., Ben-Yaakov, K., Gradus, T., Zonszain, J., Farhy, C., et al. (2016). Phosphatidylserine ameliorates neurodegenerative symptoms and enhances axonal transport in a mouse model of familial dysautonomia. PLoS Genet. *12*, e1006486.

Nagata, S. (2010). Apoptosis and autoimmune diseases. Ann. N Y Acad. Sci. *1209*, 10–16.

Nandrot, E.F., Anand, M., Almeida, D., Atabai, K., Sheppard, D., and Finnemann, S.C. (2007). Essential role for MFG-E8 as ligand for alphavbeta5 integrin in diurnal retinal phagocytosis. Proc. Natl. Acad. Sci. USA *104*, 12005–12010.

Natarajan, P., Wang, J., Hua, Z., and Graham, T.R. (2004). Drs2p-coupled aminophospholipid translocase activity in yeast Golgi membranes and relationship to in vivo function. Proc. Natl. Acad. Sci. USA *101*, 10614–10619.

Paulusma, C.C., Folmer, D.E., Ho-Mok, K.S., de Waart, D.R., Hilarius, P.M., Verhoeven, A.J., and Oude Elferink, R.P. (2008). ATP8B1 requires an accessory protein for endoplasmic reticulum exit and plasma membrane lipid flippase activity. Hepatology *47*, 268–278.

Poe, A.R., Tang, L., Wang, B., Li, Y., Sapar, M.L., and Han, C. (2017). Dendritic space-filling requires a neuronal type-specific extracellular permissive signal in *Drosophila*. Proc. Natl. Acad. Sci. USA *114*, E8062–E8071.

Rasmussen, J.P., Sack, G.S., Martin, S.M., and Sagasti, A. (2015). Vertebrate epidermal cells are broad-specificity phagocytes that clear sensory axon debris. J. Neurosci. *35*, 559–570.

Ravichandran, K.S. (2010). Find-me and eat-me signals in apoptotic cell clearance: progress and conundrums. J. Exp. Med. *207*, 1807–1817.

Ruggiero, L., Connor, M.P., Chen, J., Langen, R., and Finnemann, S.C. (2012). Diurnal, localized exposure of phosphatidylserine by rod outer segment tips in wild-type but not Itgb5-/- or Mfge8-/- mouse retina. Proc. Natl. Acad. Sci. USA *109*, 8145–8148.

Saito, K., Fujimura-Kamada, K., Furuta, N., Kato, U., Umeda, M., and Tanaka, K. (2004). Cdc50p, a protein required for polarized growth, associates with the Drs2p P-type ATPase implicated in phospholipid translocation in Saccharomyces cerevisiae. Mol. Biol. Cell *15*, 3418–3432.

Salter, M.W., and Stevens, B. (2017). Microglia emerge as central players in brain disease. Nat. Med. *23*, 1018–1027.

Scheffer, L.L., Sreetama, S.C., Sharma, N., Medikayala, S., Brown, K.J., Defour, A., and Jaiswal, J.K. (2014). Mechanism of Ca^{2+}-triggered ESCRT assembly and regulation of cell membrane repair. Nat. Commun. *5*, 5646.

Schoenmann, Z., Assa-Kunik, E., Tiomny, S., Minis, A., Haklai-Topper, L., Arama, E., and Yaron, A. (2010). Axonal degeneration is regulated by the apoptotic machinery or a NAD+-sensitive pathway in insects and mammals. J. Neurosci. *30*, 6375–6386.

Schuldiner, O., and Yaron, A. (2015). Mechanisms of developmental neurite pruning. Cell. Mol. Life Sci. *72*, 101–119.

Segawa, K., and Nagata, S. (2015). An apoptotic 'eat me' signal: phosphatidylserine exposure. Trends Cell Biol. *25*, 639–650.

Segawa, K., Suzuki, J., and Nagata, S. (2011). Constitutive exposure of phosphatidylserine on viable cells. Proc. Natl. Acad. Sci. USA *108*, 19246–19251.

Simon, D.J., Weimer, R.M., McLaughlin, T., Kallop, D., Stanger, K., Yang, J., O'Leary, D.D., Hannoush, R.N., and Tessier-Lavigne, M. (2012). A caspase cascade regulating developmental axon degeneration. J. Neurosci. *32*, 17540–17553.

Suzuki, J., Umeda, M., Sims, P.J., and Nagata, S. (2010). Calcium-dependent phospholipid scrambling by TMEM16F. Nature *468*, 834–838.

Suzuki, J., Denning, D.P., Imanishi, E., Horvitz, H.R., and Nagata, S. (2013). Xk-related protein 8 and CED-8 promote phosphatidylserine exposure in apoptotic cells. Science *341*, 403–406.

Tanaka, K., Fujimura-Kamada, K., and Yamamoto, T. (2011). Functions of phospholipid flippases. J. Biochem. *149*, 131–143.

Tang, X., Halleck, M.S., Schlegel, R.A., and Williamson, P. (1996). A subfamily of P-type ATPases with aminophospholipid transporting activity. Science *272*, 1495–1497.

Tao, J., and Rolls, M.M. (2011). Dendrites have a rapid program of injury-induced degeneration that is molecularly distinct from developmental pruning. J. Neurosci. *31*, 5398–5405.

Tufail, Y., Cook, D., Fourgeaud, L., Powers, C.J., Merten, K., Clark, C.L., Hoffman, E., Ngo, A., Sekiguchi, K.J., O'Shea, C.C., et al. (2017). Phosphatidylserine exposure controls viral innate immune responses by microglia. Neuron *93*, 574–586.e578.

Wakatsuki, S., and Araki, T. (2017). Specific phospholipid scramblases are involved in exposure of phosphatidylserine, an "eat-me" signal for phagocytes, on degenerating axons. Commun. Integr. Biol. *10*, e1296615.

Wakatsuki, S., Tokunaga, S., Shibata, M., and Araki, T. (2017). GSK3B-mediated phosphorylation of MCL1 regulates axonal autophagy to promote Wallerian degeneration. J. Cell Biol. *216*, 477–493.

Williams, D.W., Kondo, S., Krzyzanowska, A., Hiromi, Y., and Truman, J.W. (2006). Local caspase activity directs engulfment of dendrites during pruning. Nat. Neurosci. *9*, 1234–1236.

Zhu, X., Libby, R.T., de Vries, W.N., Smith, R.S., Wright, D.L., Bronson, R.T., Seburn, K.L., and John, S.W. (2012). Mutations in a P-type ATPase gene cause axonal degeneration. PLoS Genet. *8*, e1002853.

Cell Reports, Volume *24*

Supplemental Information

Phosphatidylserine Externalization Results from and Causes Neurite Degeneration in *Drosophila*

Maria L. Sapar, Hui Ji, Bei Wang, Amy R. Poe, Kush Dubey, Xingjie Ren, Jian-Quan Ni, and Chun Han

SUPPLEMENTAL INFORMATION

SUPPLEMENTAL FIGURES

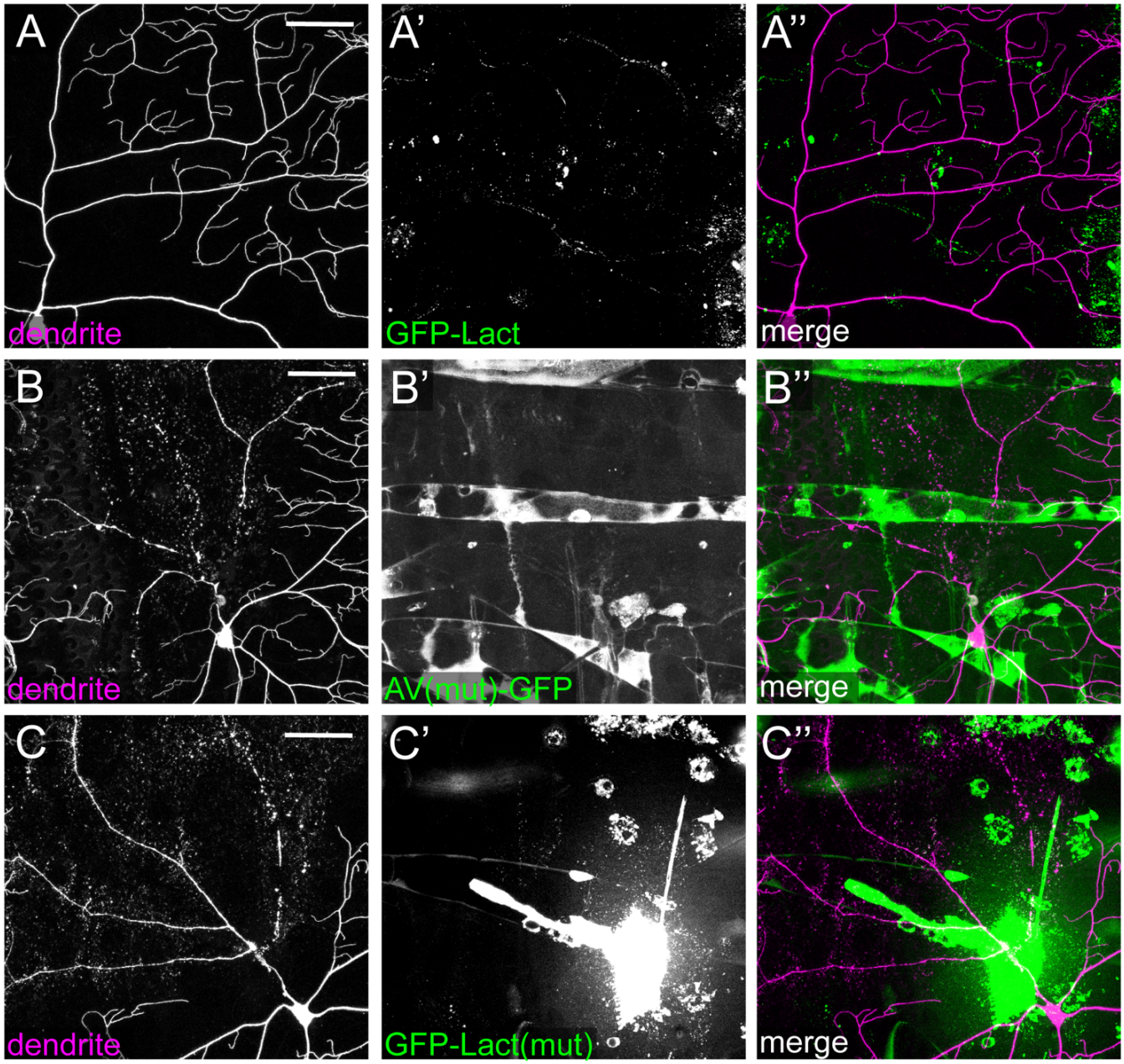

Figure S1. Mutant PS sensors do not bind to degenerating dendrites, related to Figure 1.

(A-A") An uninjured C4da neuron in the presence of Lact-GFP.

(B-B") Injured C4da dendrites in the presence of AV (mut)-GFP at 4-5 hours AI

(C-C") Injured C4da dendrites in the presence of GFP-Lact (mut) at 4-5 hours AI.

Scale bars represent 50 μm.

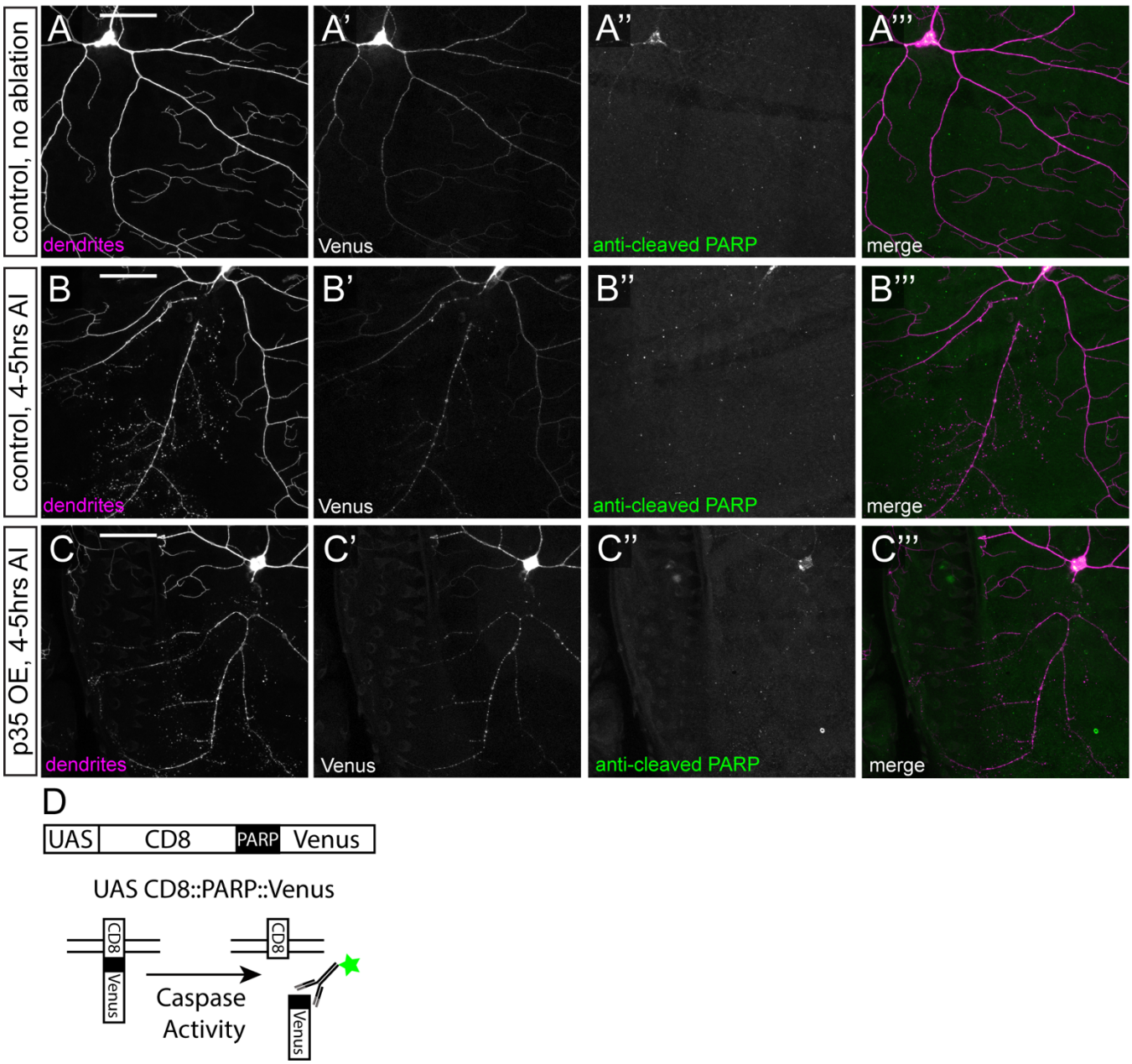

Figure S2. Injury of C4da neurons does not lead to caspase activity at 4 hrs AI, related to Figure 2.

(A-B''') Anti-cleaved PARP staining in uninjured (A-A''') and injured (B-B''') wildtype neurons.

(C-C''') Anti-cleaved PARP staining in injured p35 expressing (C-C''') dendrites.

(D) Schematic representation of CD8::PARP::Venus, the cleavage of which by caspases exposes a unique epitope that can be recognized by a specific antibody (adapted from Williams et al., 2006). The antibody appears to show some weak background binding to noncleaved PARP. Injured dendrites of neither wildtype neurons nor p35-expressing neurons showed higher than background staining.

Scale bars represent 50 μm.

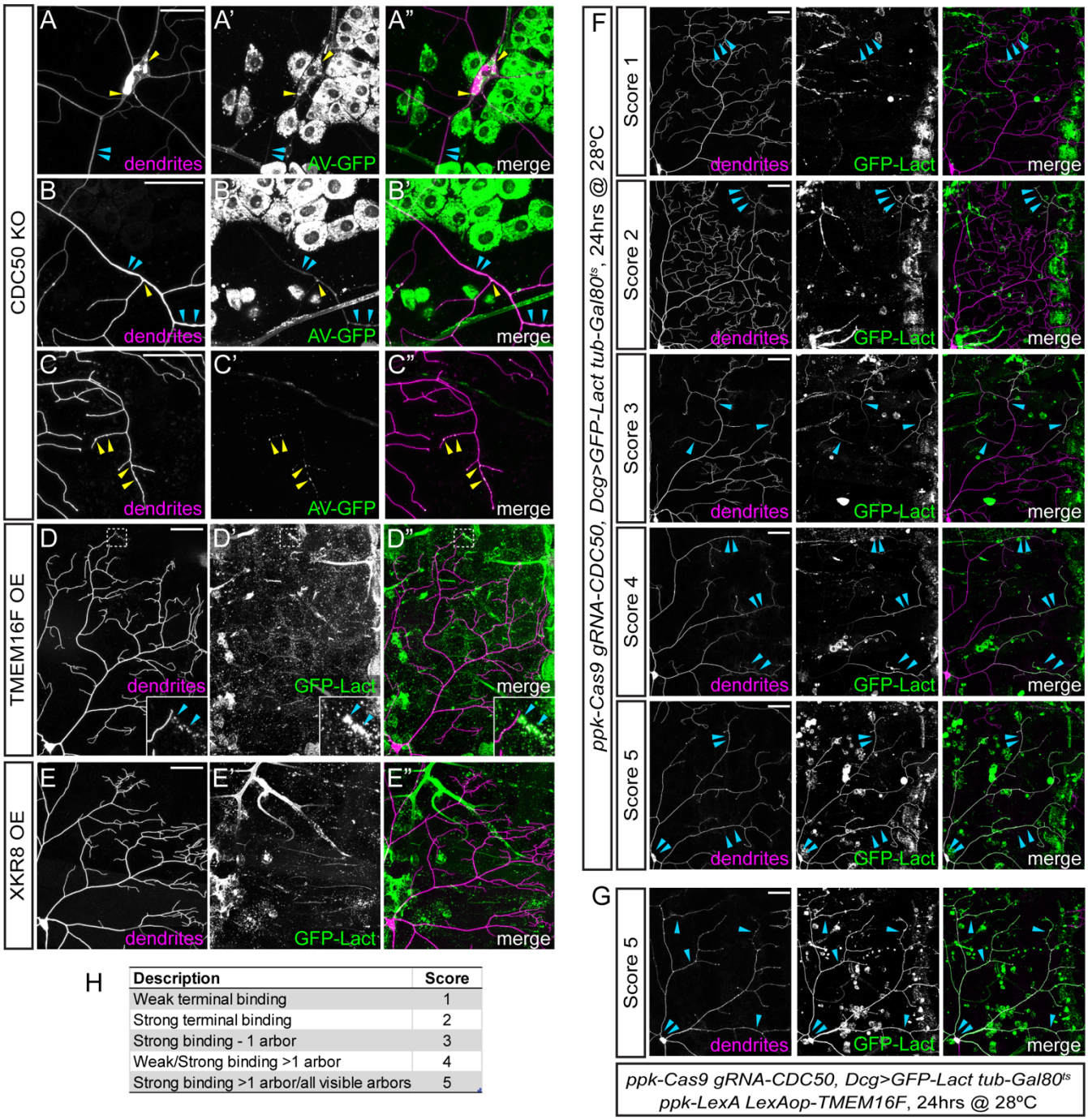

H

Description	Score
Weak terminal binding	1
Strong terminal binding	2
Strong binding - 1 arbor	3
Weak/Strong binding >1 arbor	4
Strong binding >1 arbor/all visible arbors	5

Figure S3. PS exposure on *CDC50* knockout and scramblase overexpression neurons, related to Figure 3.

(A-C) Labeling of *CDC50* KO neurons by AV-GFP, showing a cell body and primary branches (A-A"), primary branches (B-B"), distal dendrites (C-C"). Blue arrowheads point to smooth labeling and yellow arrowheads point to intracellular puncta.

(D-D") Dendrites of a TMEM16F OE neuron labeled by constitutively expressed GFP-Lact. Inset shows dendrite debris labeled by GFP-Lact.

(E) Dendrites of an XKR8 OE neuron in the presence of constitutively expressed GFP-Lact. No obvious dendrite labeling was detected.

(F) Scoring system for quantifying the binding of transiently expressed GFP-Lact on *CDC50* KO neurons and *CDC50* KO +

TMEM16F OE neurons. Representative *CDC50* KO neurons are shown. Blue arrowheads indicate GFP-Lact binding.

(G) Example of a *CDC50* KO + TMEM16F OE neuron that received a score of 5

(H) Description of GFP-Lact labeling and corresponding scores.

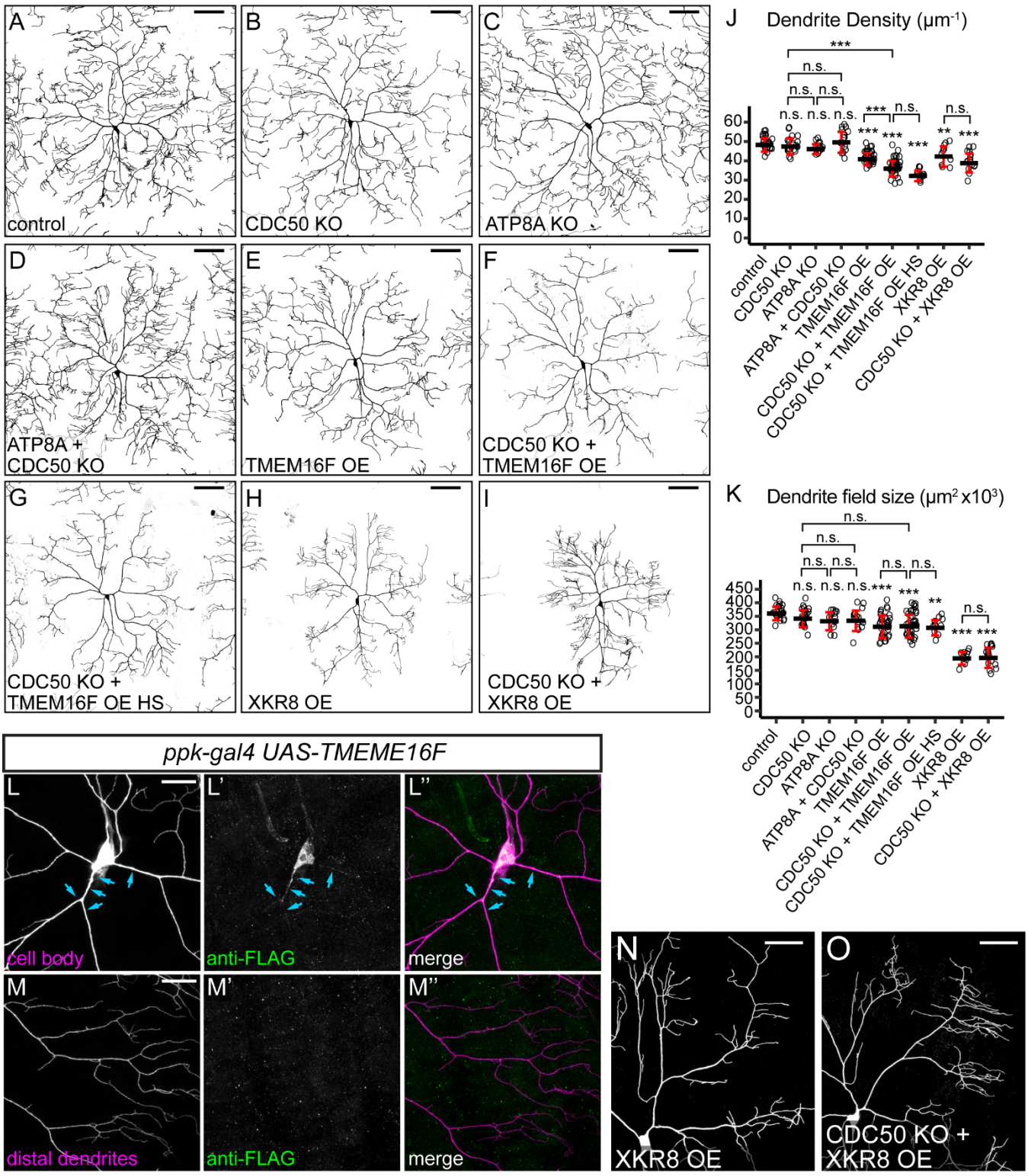

Figure S4. Dendrite morphologies of flippase knockout neurons and scramblase overexpressing neurons, related to Figure 4.

(A-I) Dendritic fields of control (A), *CDC50* KO (B), *ATP8A* KO (C), *CDC50* and *ATP8A* double KO (D), TMEM16F OE (E), *CDC50* KO + TMEM16F OE (F), heat-shocked *CDC50* KO + TMEM16F OE (G), XKR8 OE (H), and *CDC50* KO + XKR8 OE (I) neurons.

(J and K) Quantification of dendrite density (J) and dendrite field size (K) in indicated genotypes. n = number of neurons: control (n=24, 11 animals); *CDC50* KO (n=21, 11 animals); *ATP8A* KO (n=13, 9 animals); *ATP8A* + *CDC50* KO (n=16, 9 animals); TMEM16F OE (n=34, 19 animals); *CDC50* KO + TMEM16F OE (n=41, 26 animals); *CDC50* KO + TMEM16F OE HS (n=11, 7 animals); XKR8 OE (n=10, 8 animals); *CDC50* KO + XKR8 OE (n=16, 9 animals). **p≤0.01, ***p≤0.001, n.s., not significant; One-way ANOVA and Tukey's HSD test. Black bar, mean; red bars, SD.

(L-M") Anti-Flag staining of TMEM16F in the cell body and primary branches (L-L") and distal dendrites (M-M"). Blue arrows indicate anti-Flag signals.

(N-O) Partial dendritic fields of XKR8 OE (N) and *CDC50* KO + XKR8 OE (O) C4da neurons showing the level of dendritic debris in epidermal cells.

Scale bars represent 100 μm in (A-I) and 25 μm in (M) and (L) and 50 μm in (N) and (O)

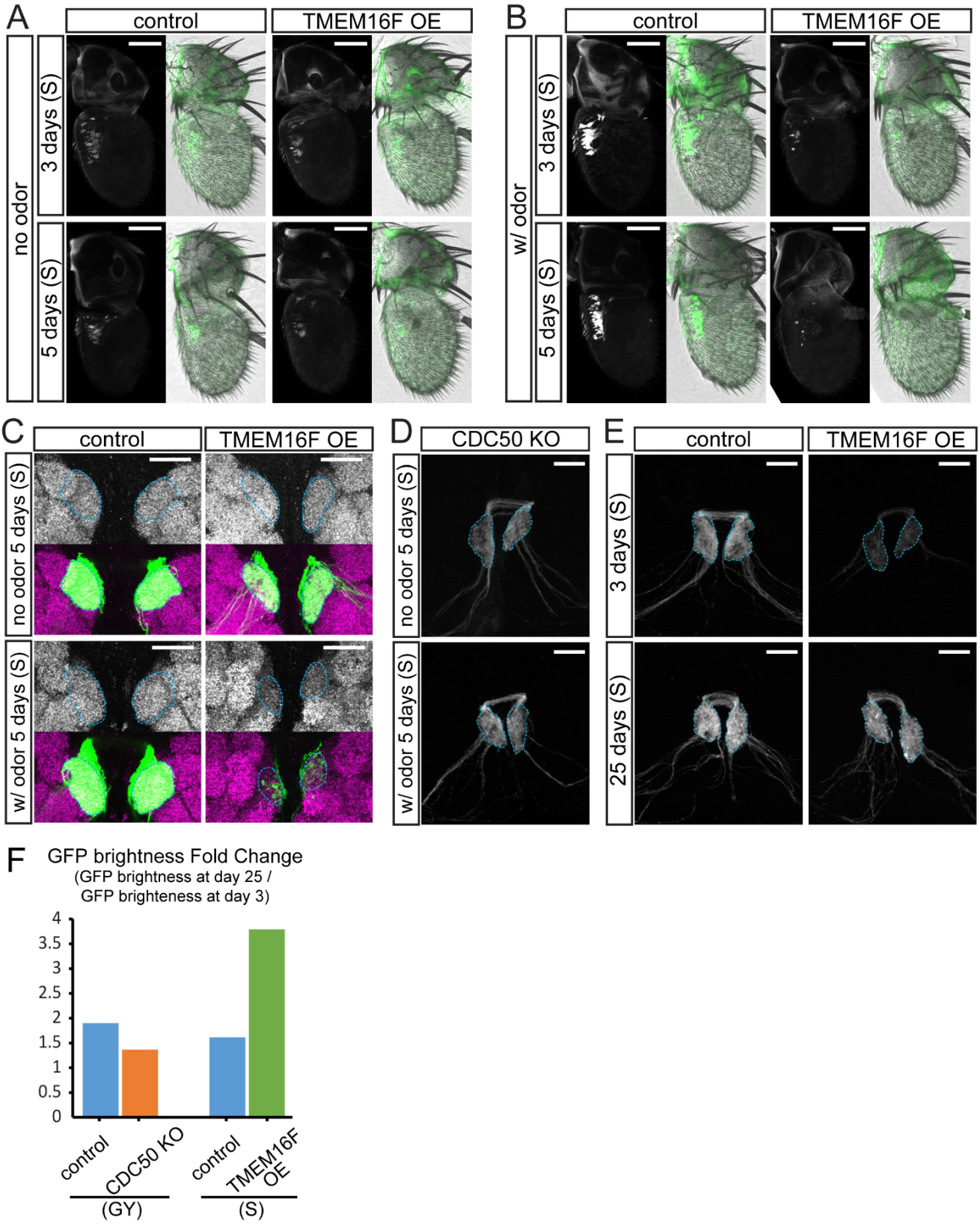

Figure S5. Flippase loss and scramblase overexpression cause distinct modes of axonal degeneration in the adult fly brain, related to Figure 6.

(A and B) Antennae of control and TMEM16F-overexpressing flies that were not exposed to odors (A) or exposed to ethyl butyrate (B) to show GFP signals at the cell bodies of Or22a ORNs.

(C) DM2 glomeruli of control and TMEM16F-overexpressing 5-day-old flies that were exposed or not exposed to ethyl butyrate. Anti-Brp (nc82) staining is in grey in each upper panel or in magenta in each merged panel. DM2 glomeruli are outlined.

(D) Axons of CDC50 KO Or22a ORNs in 5-day-old adult flies that were exposed or not exposed to ethyl butyrate.

(E) Axons of control and TMEM16F-overexpressing Or22a ORNs in 3-day-old and 25-day-old adult brains in the absence of odor exposure.

(F) Fold change of GFP levels between 3 and 25 days in genotypes shown.

The type of fly media used for each experiment is indicated: S – sucrose agar; GY – glucose yeast food. In all image panels, Or22a glomeruli are outlined. Scale bars represent 50 μm in (A and B) and 20 μm in (C-E).

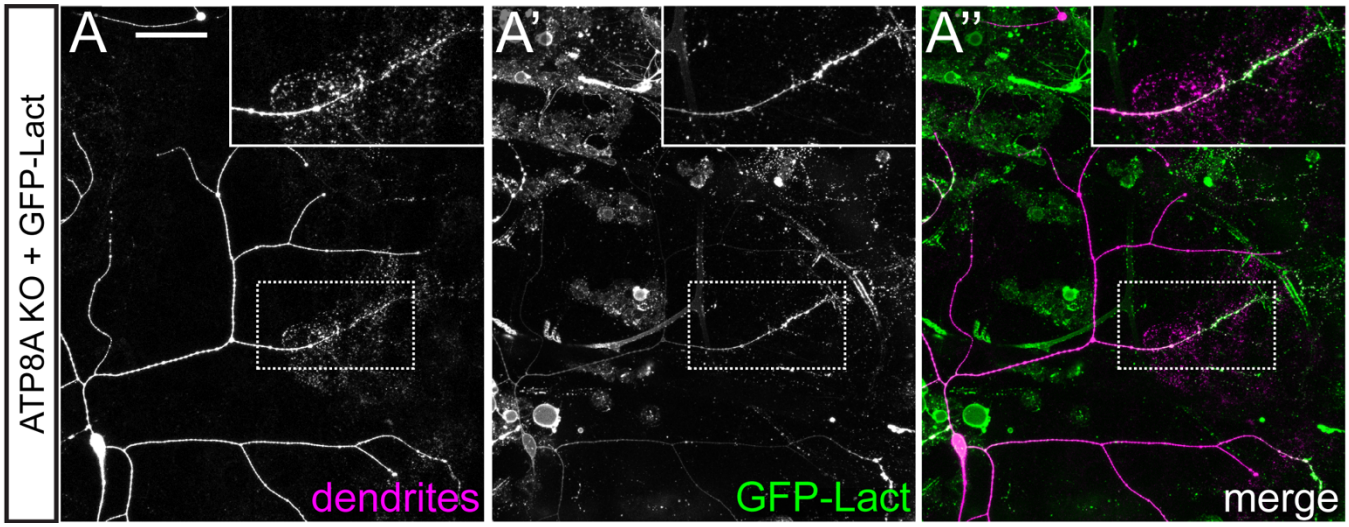

Figure S6. Constitutively expressed GFP-Lact causes *ATP8A* knockout neurons to degenerate, related to Figure 7.

(A-A") Dendrites of an *ATP8A* KO neuron in the presence of constitutively expressed GFP-Lact. Inset shows a degenerating dendrite with high GFP-Lact labeling. The scale bar represents 50 μm.

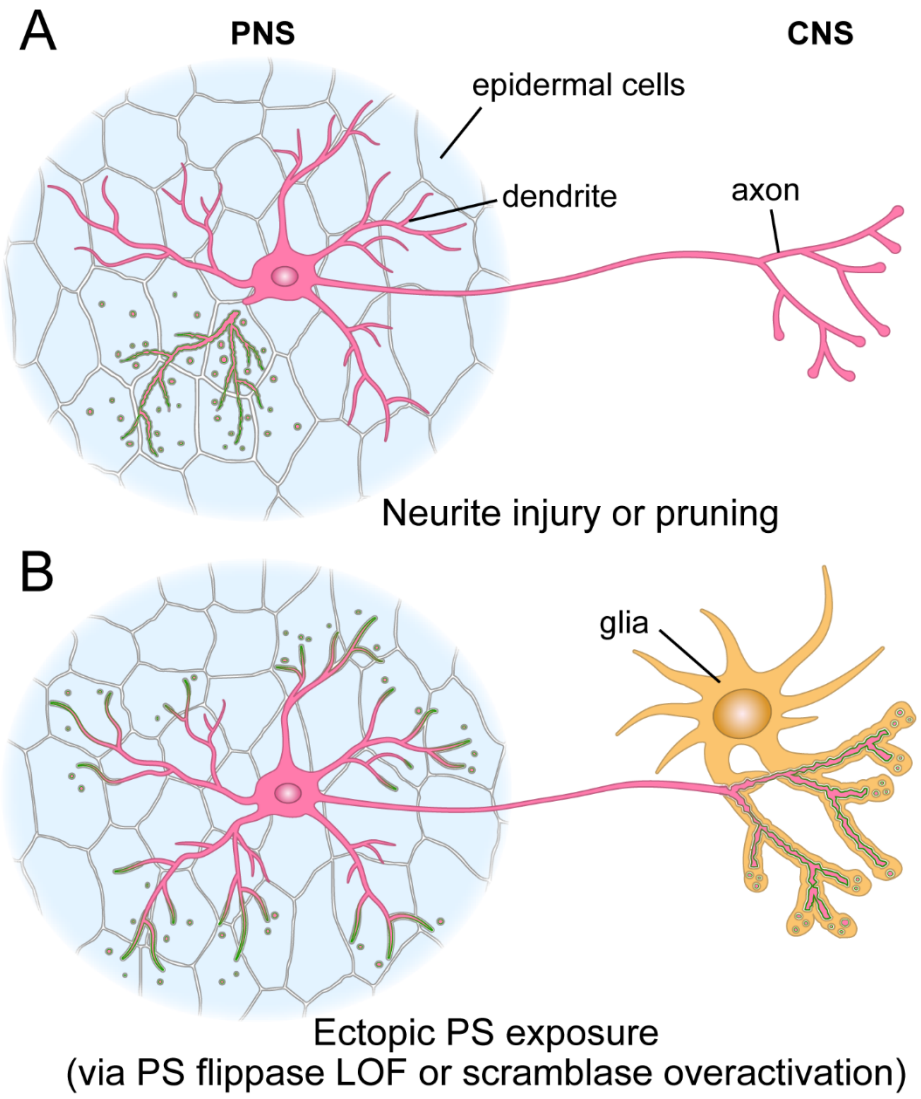

Figure S7. PS exposure is a result and a cause of neurite degeneration, related to Figure 6.

(A) During neurite injury or pruning, detached neurites expose PS (green) as an event of the degeneration program. Resident phagocytes such as epidermal cells recognize PS-exposing neurites and engulf neurite debris.

(B) Loss of PS flippases or overactivation of scramblases result in PS exposure on distal neurites, which causes resident phagocytes, such as epidermal cells in the PNS and glia in the CNS, to attack and break down PS-exposing neurites. The involvement of glia in this model is inferred from previous studies (MacDonald et al., 2006; Freeman, 2015).

SUPPLEMENTAL EXPERIMENTAL PROCEDURES

Fly strains

ppk-CD4-tdTom (Han et al., 2011), *ppk-MApHS* (Han et al., 2014), *ppk-Gal4* (Han et al., 2012), *UAS-CD4-tdTom* (Han et al., 2011), *tubP-Gal80^{ts}* (McGuire et al., 2003), *ppk-LexA* (Poe et al., 2017), *Dcg-Gal4* (Suh et al., 2006), *UAS-Wld^{s}* (MacDonald et al., 2006), *Or22a-Gal4* (Dobritsa et al., 2003), and *UAS-mCD8-GFP* (Lee and Luo, 1999) have been previously described. *UAS-p35* (BDSC 5072) and *UAS-Diap1* (BDSC 6657) were obtained from Bloomington Stock Center (BDSC).

Molecular cloning and transgenic flies

UAS-driven PS sensors were constructed in pIHEU-MCS (Addgene 58375), an insulated high-expression UAS vector that is compatible with both φC31-mediated integration and P-element-mediated transformation. pIHEU contains 5xUAS, a HIH cassette (*hsp70* core promoter-5′UTR, a chimeric intron, and *His2Av* 3′UTR-polyA) that supports high transgene expression in *Drosophila* (Han et al., 2011), and two copies of gypsy insulators that reduce positional effect-related leaky expression. To construct pIHEU-MCS, an SphI-XbaI fragment was isolated from pACU2 (Han et al., 2011) and cloned into SphI/XbaI sites of pAPIC-CD4-tdGFP (Han et al., 2011).

UAS-AV-GFP and *UAS-AV(mut)-GFP*: From 5' to 3', a Syn21-Akh SP fragment, human Annexin V (AV) coding sequence, and superfolder GFP (sfGFP) coding sequence were cloned into pIHEU-MCS between EcoRI/XbaI sites. Syn21 (aacttaaaaaaaaaaatcaaa) (Pfeiffer et al., 2012) is a translation enhancer sequence before the start codon. Akh SP (Han et al., 2011) encodes a signal peptide for AV-GFP secretion. AV and AV(mut) fragments were PCR-amplified from pJM31AnxV::GFP and pJM62 AnxVMut::GFP (Mapes et al., 2012) (gifts from Ding Xue, University of Colorado Boulder), respectively, using primers aaaagctagcGCACAGGTTCTCAGAGGC and aaaaaagcttGTCATCTTCTCCACAGAGCAG and subsequently digested by NheI and HindIII. sfGFP was PCR-amplified from pBS-sfGFP (a gift from Thomas Kornberg, University of California, San Francisco) using primers aaaaaagcttggtggcggcggaagtggaggtggaggctcgATGTCCAAGGGCGAGGAG and aatttctagaTTACTTGTACAGCTCATCCATGCCCAG and subsequently digested by HindIII and XbaI.

UAS-GFP-Lact and *UAS-GFP-Lact(mut)*: From 5' to 3', the Syn21-Akh SP fragment, sfGFP coding sequence, and mouse lactadherin (Lact) C1C2 coding sequence were cloned into pIHEU-MCS between EcoRI/XbaI sites. sfGFP was PCR-amplified from pBS-sfGFP using primers ataagctagcagtATGTCCAAGGGCGAGGAG and aaaaaagcttcgagccaccaccgccacttccgccgccaccggaCTTGTACAGCTCATCCATGCCCAG and subsequently digested by NheI and HindIII. LactC1C2 and LactC1C2(mut) were PCR-amplified from pJM483 GFP::LactC1C2 and pJM656 GFP::LactC1C2(Mut) (Mapes et al., 2012) (gifts from Ding Xue, University Colorado Boulder), respectively, using primers aaaaaagcttCGCTGTTCTACACAGCTGGGCATGGAAGGGGG and aatttctagaTTAACAGCCCAGCAGCTCCAG and subsequently digested by HindIII and XbaI.

UAS-AV-mCard: Syn21-Akh SP-AV and mCardinal (mCard) coding sequence (Chu et al., 2014) were cloned into EcoRI/XbaI sites of pIHEU-MCS. The Syn21-Akh SP-AV fragment was isolated from pIHEU-AV-sfGFP by EcoRI/HindIII digestion. The mCard fragment was PCR-amplified from pcDNA3-mCardinal (Addgene 51311) using primers aaaaaagcttggtggcggcggaagtggaggtggaggctcgATGGTGAGCAAGGGCGAGG and aatttctagaTTACTTGTACAGCTCGTCCATGCC and subsequently digested by HindIII/XbaI.

LexAop-GFP-Lact: An Syn21-Akh SP-AV-sfGFP fragment was isolated from pIHEU-AV-sfGFP by EcoRI/XbaI digestion and then cloned into EcoRI/XbaI sites of pAPLO (Poe et al., 2017).

LexAop-AV-mCard: The Syn21-Akh SP-AV-mCard fragment was isolated from pIHEU-AV-mCard by EcoRI/XbaI digestion and cloned into EcoRI/XbaI sites of pAPLO.

UAS-XKR8 and UAS-TMEM16F were constructed in pACUH (Addgene 58374), a UAS vector that is compatible with both φC31-mediated integration and P-element-mediated transformation. pACUH contains 10xUAS, *hsp70* core promoter-5′UTR, and *SV40* 3′UTR-polyA, and drives weaker transgene expression than pIHEU-MCS. To construct pACUH, a fragment containing the attB sequence was first inserted into the NdeI site of pUAST (Brand and Perrimon, 1993) to make pACU. The 5xUAS in pACU was then replaced with a 10xUAS fragment.

UAS-XKR8: XKR8-Flag coding sequence was PCR-amplified from pMXs-puro mXkr8-GFP (a gift from Shigekazu Nagata, Osaka University) using primers aaaaGAATTCaaaATGCAGATGATGACTAGGAAGGTCC and aattTCTAGAttacttgtcgtcgtcgtccttgtagtcgccGAGGACTCCATTCAGCTGCACCTCCTCTGTC, and subsequently cloned into EcoRI/XbaI sites of pACUH.

UAS-TMEM16F: TMEM16F-D430G-L-Flag coding sequence was PCR-amplified from pMXs-puro mTMEM16F D430G-L FLAG (a gift from Shigekazu Nagata, Osaka University) using primers aaaaGAATTCaaaATGCAGATGATGACTAGGAAGGTCC and aaaaGAATTCaaaATGCAGATGATGACTAGGAAGGTCC, and subsequently cloned into EcoRI/XbaI sites of pACUH.

LexAop-Xkr8 and *LexAop-TMEM16F*: XKR8-Flag and TMEM16F D430G-L-Flag were isolated from pACUH-Xkr8-Flag and pACUH-TMEM16D430G-Flag, respectively, by EcoRI/XbaI digestion and cloned into EcoRI/XbaI sites of pAPLO3. pAPLO3 is similar to pAPLO but only has 11x LexAop2 and no intron. pAPLO3 is expected to drive lower transgene expression than pAPLO.

R16A03-lexA: The R16A03 enhancer was PCR amplified from R16A03-Gal4 (BDSC 45809) genomic DNA using primers ggggACAAGTTTGTACAAAAAAGCAGGCTGGGGAGAGTTGCCGTATCATTTTGGCTTATTGG and ggggACCACTTTGTACAAGAAAGCTGGGTGTCTCGACTAGCTTCCTGCTCAACCTGC. The resultant DNA fragment was used to create an entry vector through a Gateway BP reaction (Thermo Fisher Scientific). The entry vector was then combined with pBPLexA::p65Uw (Addgene 26231) to generate pR16A03-LexAp65 expression vector through a Gateway LR reaction.

The above constructs were injected in house or by Rainbow Transgenic Flies to transform flies through φC31 integrase-mediated integration into attP docker sites.

Generation of *drpr^{indel}* allele by CRISPR/Cas9

A gRNA-drpr expression vector was constructed using the U6b-sgRNA-short vector (Ren et al., 2013) and the targeting sequence GGTAATCCTCATAGCCTGCC. gRNA-drpr plasmid DNA was then injected into *nos-Cas9^{attP2}* embryos. The resulting flies were crossed with TM6B balancer flies to isolate individual progeny carrying mutations at the targeting sequence. Indel mutations were detected by the loss of a BglI site in genomic PCR products amplified by primers ACGTCATAAACTCATCCGACGGG and CCAACTCACCACAACAGTCCCTC. Sequencing of *drpr^{indel}* homozygous flies confirmed that 2 nucleotides (CT) were inserted after the T in the 9th codon, causing a reading frame shift mutation. Because the next in-frame methionine codon (AA143) is after the signal peptide (AA1-AA30), alternatively translated proteins should not be properly processed and targeted to the plasma membrane. Therefore, *drpr^{indel}* is predicted to behave as a null allele.

Tissue-specific gene knockout via CRISPR/Cas9

Tissue-specific gene knockout in C4da neurons was achieved by crossing flies carrying *ppk-Cas9* and flies ubiquitously expressing two gRNAs targeting the gene of interest. *ppk-Cas9* is similar to *ppk-CD4-tdTom* except that the coding sequence is from *S. pyogenes* Cas9 gene. The transgenic gRNA constructs were similar to pCFD4-U6.1_U6.3 except that the selection marker is mini-white (Port et al., 2014). The details of the construction and characterization of *ppk-Cas9* and gRNA vectors will be published elsewhere. For tissue-specific gene knockout in adult Or22a ORNs, *Or22a-Gal4* was used to drive *UAS-Cas9* expression so that CRISPR/Cas9-mediated knockout only occurred in mature neurons.

We used two gRNA predictor tools, sgRNA Scorer 2.0 (https://crispr.med.harvard.edu) and Benchling (www.benchling.com), to identify candidate gRNA targeting sequences with high on-target scores in both algorithms. For each gene, we selected two targeting sequences that are against coding exons of all splicing isoforms and are predicted not to have alternative target sites by both algorithms. The targeting sequences are GGTGTGGTATACATGTACTACGG and GTCAAGTTCCGAAACCCAGAGGG for *CDC50* and ATCATCTGCATCGTACCCAGCGG and AAGTTCGCGAGCAACTTCCGCGG for *ATP8A* (the PAM sequences are underlined and not included in the final gRNA vectors). The constructs were injected by Rainbow Transgenic Flies to transform attP docker lines using φC31 integrase-mediated transformation, with *gRNA-CDC50* inserted to *attP^{2}* and *gRNA-ATP8A* inserted to *attP^{VK19}*.

Testing gRNA efficiency

To test gRNA efficiency, homozygous males of gRNA for target gene were crossed to *Act-Cas9 lig4* homozygous females. The embryo density was controlled (around 100 embryos per vial) and the vials were monitored every day to record the animal lethal phase. As *Act-Cas9* and the *lig4* null mutation are both on the X chromosome, the male progeny from the cross is *lig4* deficient and therefore cannot repair DNA double-stranded breaks (DSBs) through NHEJ. In contrast, the female progeny is heterozygous for *lig4* and thus can repair DSBs. Efficient gRNAs will target the gene locus to create bi-allelic DSBs, which will be repaired to generate indels in female somatic cells but left unrepaired in male somatic cells. If target gene is a non-essential gene, female progeny with indel mutations at the gene locus should be viable while male progeny will die in the pupal stage due to the lack of the DSB repair. If target gene is an essential gene, target gene LOF will cause both female and male progeny to die to at a stage similar to the lethal phase of target gene zygotic null mutants. Viable male progeny from this cross indicates inefficient gRNAs. It is also possible, if the gRNA is inefficient but the gene is essential, female progeny may survive. The *gRNA-CDC50* efficiency test resulted in lethality at 1st to 2nd instar larval stages for most animals and rarely at 3rd instar, suggesting that the gRNA line is efficient. For *gRNA-ATP8*, only adult females emerged. It possible that ATP8 is a nonessential gene and the gRNA line is very efficient, or that *ATP8A* is an essential gene but the gRNA line is only moderately efficient.

Live imaging

Animals were reared at 25°C in density-controlled vials (60-100 embryos/vial) on standard yeast-glucose medium (doi:10.1101/pdb.rec10907). Larvae at 125 hours AEL (wandering stage) were mounted in 100% glycerol under coverslips with vacuum grease spacer and imaged using a Leica SP8 microscope equipped with a 20X NA0.75 multi-immersion

objective for quantifying dendritic field sizes and length and a 40X NA1.30 oil objective for others. For imaging with the 40X objective, larvae were lightly anesthetized with isoflurane before mounting. For consistency, we imaged dorsal ddaC neurons from A1-A3 segments (2-3 neurons per animal) on one side of the larvae. For imaging GFP-Lact labeling of *CDC50* KO and *CDC50* KO + TMEM16F OE neurons, we imaged ddaC neurons on both sides of the larvae and hence 3-5 neurons per animal. Unless stated otherwise, confocal images shown in all figures are maximum intensity projections of z stacks encompassing the epidermal layer and the sensory neurons beneath, which are typically 8–10 μm for larvae and 12–15 μm for pupae.

Injury assay

For dendrite lesion, larvae at 90 hr AEL were lightly anesthetized with isoflurane, mounted in a small amount of halocarbon oil (Halocarbon Products Corporationt) under coverslips with grease spacers. The laser ablation was performed on a Zeiss LSM880 Confocal/Multiphoton Upright Microscope, using a 790 nm two-photon laser at primary dendrites of ddaC neurons in A1 and A3 segments. The laser power was set at 80% and number of laser pulses/iterations = 20. Animals were recovered on grape juice agar plates following lesion for appropriate time (4-5 hr or 9-10 hr). After recovery, the larvae were either mounted in 100% glycerol under coverslips with grease spacers and imaged using a Leica SP8 microscope or imaged with the long-term time-lapse imaging method.

Long-term time-lapse imaging

Long-term time-lapse imaging at the larval stage was done as described previously (Poe et al., 2017) with small modifications. Briefly, a layer of double-sided tape was placed on the coverslip to define the position of PDMS blocks. A small amount of UV glue was added to the groove of PDMS and to the coverslip. Anesthetized larvae were placed on top of the UV glue on the coverslip and then covered by PDMS blocks with the groove side contacting the larva. Glue was then cured by 365nm UV light. The coverslip with attached PDMS and larvae was mounted on an aluminum slide chamber that contained a piece of moisturized Kimwipes (Kimtech Science) paper. Time-lapse imaging was performed on a Leica SP8 confocal with a 40x NA1.3 oil objective at digital zoom 0.75 and a 3-min interval. For ablation experiments, larvae were recovered after injury on grape agar plates for 1.5-2 hours before mounting and imaging. For long-term time-lapse imaging of dendrite pruning, white pupae were directly mounted in the imaging chamber similar to larval mounting and kept on the imaging chamber for 4-6 hours before imaging.

Antenna imaging

Flies were washed in ethanol, the antennae were removed, allowed to briefly dry and then were mounted in 100% glycerol on charged Diamond White Glass microscope slides (Globe Scientific, 1358W) with vacuum grease (Dow Corning) as spacers between coverslips and slides. The antennae were imaged under Leica SP8 microscope with a 40x NA1.3 oil objective.

Transient expression of GFP-Lact

Animals expressing *dcg-Gal4 UAS-GFP-Lact* and *tubP-Gal80ts* were kept at 18°C until late 3rd instar. The vials were then transferred to and kept in 28°C incubator for 24 hours. Wandering larvae were then selected from the vials for imaging. For injury after induction of GFP-Lact, animals were laser injured after 32-hour incubation at 28°C and then were recovered on grape agar plates for 3-4 hours at 28°C before imaging.

Larval heat shock treatment

Larvae at 125 hours AEL were placed in a chamber made of two opposing 35 mm petri dishes which was sealed with Parafilm (Bemis NA). The chamber was then subject to three 2-min heat shocks in 42°C water bath with 10-min intervals. Larvae were then recovered on moisturized petri dishes for 30 min at 25°C before imaging.

Labeling of PS exposure

To visualize in vivo PS exposure in larvae or pupae, we used the following combinations of drivers and PS sensors for each experiment. For injury and pruning: *Dcg-Gal4 UAS-AV-GFP* or *Dcg-Gal4 UAS-GFP-Lact*; for overexpression of Wld^{s}, p35, or Diap1: *R16A03-LexA LexAop-GFP-Lact* with *ppk-Gal4 UAS-Wld^{s}*, *UAS-p35*, *or UAS-Diap1*; for examining PS exposure due to *CDC50*/*ATP8* KO: *Dcg-Gal4 UAS-AV-GFP* or *Dcg-Gal4 UAS-GFP-Lact* with *ppk-Cas9 gRNA*; for PS exposure due to TMEM16F/XKR8 OE: *R16A03-LexA LexAop-AV-mCard* or *LexAop-GFP-Lact* with *ppk-Gal4 UAS-TMEM16F*, *or UAS-XKR8*; for *CDC50* KO + TMEM16 OE: *Dcg-Gal4 UAS-GFP-Lact*, ppk-LexA LexAop-TMEM16F, and *ppk-Cas9 gRNA-CDC50*.

Some experiments involving multiple genetic components, which required the use of recombinant flies containing both the driver and the PS sensor in genetic crosses. Because recombination of Annexin V with either Gal4 or LexA driver yielded animals with low fecundity, we used GFP-Lact only for those experiments.

Adult brain experiments

For experiments examining Or22a axon degeneration in *CDC50* KO animals, newly emerged adults were kept at 25°C for 3 days or 25 days on glucose-yeast medium prior to dissection. For experiments examining Or22a axon degeneration in TMEM16F OE animals, newly emerged adults were kept at 25°C for 3 days or 25 days on sucrose (8%) agar medium prior to dissection. For odor test, 20µl of 1% (v/v) ethyl butyrate dissolved in mineral oil was dotted on a small piece of filter paper, which was then placed on the top of sucrose (8%) agar medium in fly vials. As a control, 20 µl of mineral oil was dotted on filter paper. Newly emerged adults were separated into two groups: experimental groups were kept in vials with ethyl butyrate filter paper; control groups were kept in vials with mineral oil paper. All animals were transferred to fresh vials every day for 5 days prior to dissection. For all brain experiments, we did not detect difference between male and female brains but we only showed results from male brains for consistency.

Brain dissection was performed in PBST (0.2% Triton-X in PBS). Dissected brains were fixed in 4% formaldehyde in PBS for 20 min and then rinsed with PBST three times. Same staining protocol was used for brains as for larval body walls. Brains were mounted in SlowFade® Diamond Antifade Mountant (Thermo Fisher Scientific) on charged Diamond White Glass microscope slides (Globe Scientific, 1358W) with vacuum grease (Dow Corning) as spacers between coverslips and slides. The brains were imaged under Leica SP8 microscope with a 40x NA1.3 oil objective.

Immunohistochemistry

The antibodies used in this study are mouse monoclonal Anti-FLAG M2 antibody (Sigma F3165, 1:250), rabbit anti-cleaved PARP1 antibody(Abcam ab2317, 1:500), mouse anti-Brp (NC82) (Developmental Studies Hybridoma Bank , 1:100), rabbit anti-GFP secondary antibody conjugated to Alexa Fluor 488 (Life Technologies A-21311, 1:500), and donkey secondary antibody conjugated to Alexa Fluor 488 (Jackson ImmunoResearch 715-545-150, 1:400) or Alexa Fluor 647 (Jackson ImmunoResearch 711-605-152, 1:400). Immunostaining of *Drosophila* larval body walls was performed as previously described (Poe et al., 2017). Briefly, 3rd instar larvae were dissected in cold PBS, fixed in 4% formaldehyde/PBS for 30 min at room temperature, and stained with the primary antibody overnight at 4°C and subsequently the secondary antibody for 2 hours at room temperature. Fillets were then mounted for microscopy. For brain staining, same immunohistochemistry protocol was followed as for larva body wall staining. The brains were imaged under Leica SP8 microscope with a 40x NA1.3 oil objective.

Image analysis and quantification

Image processing and analyses were done in Fiji/ImageJ. Methods for tracing and measuring C4da neuron dendrites have been previously described (Poe et al., 2017). For dendrite debris measurement, each Z-projected image (1,024 x 1,024 pixels) taken with a 40X objective was first processed to generate a dendrite mask through Gaussian Blur (Sigma: 1), Auto Local Threshold (Phansalkar method, radius: 50), Particles8 plugin (to remove particles smaller than 200 pixels), and Dilate (iterations=2, count=1). The signals within the dendrite mask were removed and the debris outside the dendrite mask was converted to a debris mask by thresholding with fixed thresholds (40, 255). The region of interest (ROI) for measurement was defined as the area within one-epidermal-cell diameter (40 µm) from dendrites in the dorsal posterior quadrant of the ddaC dendritic field. We only considered the region within one-epidermal-cell diameter (40 µm) from dendrites in order to correct for situations in which dendrites are very sparse. The dendrite pixel area (A_{den}) and debris pixel area (A_{deb}) in the ROI were measured and dendrite coverage ratio was calculated based on the following formula: $A_{deb} \cdot A_{ROI} / (A_{ROI} - A_{den}) \cdot A_{den}$. To measure debris level in relation to the distance from the cell body, we used the Sholl Analysis plugin (https://imagej.net/Sholl_Analysis) on dendrite and debris masks. Debris particle numbers and (terminal) dendrite numbers were averaged from multiple neurons at every distance. The graphs in Figure 4M plotted average debris particle numbers divided by average dendrite numbers (left panel) or by average terminal dendrite numbers (right panel). The polynomial fits were generated by the Sholl Analysis plugin. For measuring GFP-Lact labeling, a dendrite/debris mask was generated by thresholding the tdTom channel using fixed threshold (100, 255) for every Z slice. This mask was used to extract signals from the Lact-GFP channel in each Z slice. The resultant image stack was then maximum-projected for measuring Lact-GFP intensity on selected dendritic branches within the dendrite/debris mask. For measuring Lact-GFP background levels, empty epidermal regions in the maximum projection of the original image stack were selected. We measured 2 regions on dendrites and one region in the background for each image. For kymographs, we used a custom macro based on the Straighten function to extract 4-pixel wide area centered at selected dendrites. The maximum intensity pixel in the 4-pixel area at each distance

was used to generate a single-pixel line for each time frame. The final kymographs were displayed using the Fire lookup table (LUT).

Statistical Analysis

R was used to conduct statistical analyses and generate graphs. (*$p < 0.05$, **$p < 0.01$, and ***$p < 0.001$). Statistical significance was set at $p < 0.05$. Data acquisition and quantification were performed non-blinded. Acquisition was performed in ImageJ (batch processing for debris coverage and level, manually by hand for GFP-Lact binding) and Microsoft Excel, statistical analyses were performed using R. We used the following R packages: car, stats, multcomp for statistical analysis and ggplot2 for generating graphs. Some graphs were made in Excel using its native plotting functions. For the statistical analysis we ran the following tests, ANOVA (followed by Tukey's HSD) when depended variable was normally distributed and there was approximately equal variance across groups. When dependent variable was not normally distributed and variance was not equal across groups, we used Kruskal-Wallis (followed by Dunn's test) to test the null hypothesis that assumes that the samples (groups) are from identical populations. To check for whether the data fit a normal distribution, we generated qqPlots where we plotted all of the estimated residuals which are differences between expected versus observed values. We used the Levene test to check for equal variance within groups. For comparison between two groups we used a pairwise t-test, p-values adjusted with the Bonferroni method. Fisher's exact test was used to compare experimental percentages to controls using GraphPad's online tool (https://www.graphpad.com/quickcalcs/contingency1.cfm).

Replication

For all larval and adult imaging experiments, at least 3 biological replications were performed for each genotype and/or condition.

SUPPLEMENTAL REFERENCES

Brand, A.H., and Perrimon, N. (1993). Targeted gene expression as a means of altering cell fates and generating dominant phenotypes. Development 118, 401-415.

Chu, J., Haynes, R.D., Corbel, S.Y., Li, P., Gonzalez-Gonzalez, E., Burg, J.S., Ataie, N.J., Lam, A.J., Cranfill, P.J., Baird, M.A., *et al.* (2014). Non-invasive intravital imaging of cellular differentiation with a bright red-excitable fluorescent protein. Nat Methods 11, 572-578.

Dobritsa, A.A., van der Goes van Naters, W., Warr, C.G., Steinbrecht, R.A., and Carlson, J.R. (2003). Integrating the molecular and cellular basis of odor coding in the Drosophila antenna. Neuron 37, 827-841.

Han, C., Jan, L.Y., and Jan, Y.N. (2011). Enhancer-driven membrane markers for analysis of nonautonomous mechanisms reveal neuron-glia interactions in Drosophila. Proc Natl Acad Sci U S A 108, 9673-9678.

Han, C., Song, Y., Xiao, H., Wang, D., Franc, N.C., Jan, L.Y., and Jan, Y.N. (2014). Epidermal cells are the primary phagocytes in the fragmentation and clearance of degenerating dendrites in Drosophila. Neuron 81, 544-560.

Han, C., Wang, D., Soba, P., Zhu, S., Lin, X., Jan, L.Y., and Jan, Y.N. (2012). Integrins regulate repulsion-mediated dendritic patterning of drosophila sensory neurons by restricting dendrites in a 2D space. Neuron 73, 64-78.

Lee, T., and Luo, L. (1999). Mosaic analysis with a repressible cell marker for studies of gene function in neuronal morphogenesis. Neuron 22, 451-461.

MacDonald, J.M., Beach, M.G., Porpiglia, E., Sheehan, A.E., Watts, R.J., and Freeman, M.R. (2006). The Drosophila cell corpse engulfment receptor Draper mediates glial clearance of severed axons. Neuron 50, 869-881.

Mapes, J., Chen, Y.Z., Kim, A., Mitani, S., Kang, B.H., and Xue, D. (2012). CED-1, CED-7, and TTR-52 regulate surface phosphatidylserine expression on apoptotic and phagocytic cells. Curr Biol 22, 1267-1275.

McGuire, S.E., Le, P.T., Osborn, A.J., Matsumoto, K., and Davis, R.L. (2003). Spatiotemporal rescue of memory dysfunction in Drosophila. Science 302, 1765-1768.

Pfeiffer, B.D., Truman, J.W., and Rubin, G.M. (2012). Using translational enhancers to increase transgene expression in Drosophila. Proc Natl Acad Sci U S A 109, 6626-6631.

Poe, A.R., Tang, L., Wang, B., Li, Y., Sapar, M.L., and Han, C. (2017). Dendritic space-filling requires a neuronal type-specific extracellular permissive signal in Drosophila. Proc Natl Acad Sci U S A 114, E8062-E8071.

Port, F., Chen, H.M., Lee, T., and Bullock, S.L. (2014). Optimized CRISPR/Cas tools for efficient germline and somatic genome engineering in Drosophila. Proc Natl Acad Sci U S A 111, E2967-2976.

Ren, X., Sun, J., Housden, B.E., Hu, Y., Roesel, C., Lin, S., Liu, L.P., Yang, Z., Mao, D., Sun, L., *et al.* (2013). Optimized gene editing technology for Drosophila melanogaster using germ line-specific Cas9. Proc Natl Acad Sci U S A 110, 19012-19017.

Suh, J.M., Gao, X., McKay, J., McKay, R., Salo, Z., and Graff, J.M. (2006). Hedgehog signaling plays a conserved role in inhibiting fat formation. Cell Metab 3, 25-34.